The Pennsylvania State University
The Graduate School

ELECTROMAGNETIC MODELING OF NANOWIRES AT INFRARED AND OPTICAL WAVELENGTHS

A Thesis in
Electrical Engineering
by
Michael Emile Pellen

Submitted in Partial Fulfillment
of the Requirements
for the Degree of

Master of Science

August 2008

The thesis of Michael Emile Pellen was reviewed and approved* by the following:

Douglas H. Werner
Professor of Electrical Engineering
Thesis Advisor

Pingjuan L. Werner
Associate Professor of Electrical Engineering

W. Kenneth Jenkins
Professor of Electrical Engineering
Head of the Department of Electrical Engineering

*Signatures are on file in the Graduate School.

Abstract

Nanotechnology is a rapidly growing area of research. The ability to manipulate materials at the nanometer scale through lithographic techniques such as electron-beam lithography has made it possible to generate higher density integrated circuits. Nanoscale wires, known as nanowires, have also been created using template-assisted synthesis and vapor-liquid-solid growth techniques. In order to design devices using these nanoscale structures, methods for analyzing these structures need to be developed. The methods developed for device analysis must also incorporate the behavior of materials at the infrared and optical frequencies. This thesis will develop models for analyzing nanowires in the infrared and optical spectrum by examining scattering from semiconducting nanowires and developing surface impedance models for inclusion to the method of moments.

The dispersive nature of metals and semiconductors at infrared and optical wavelengths is introduced into our modeling approaches using oscillator models. The oscillator model that was used in this work is the Lorentz-Drude oscillator model. The Lorentz-Drude oscillator model was used to represent the dielectric properties of metals such as gold and silver in the infrared and optical spectrum. Oscillator models do not exist for all materials. Particle swarm optimization was applied to parameter fit a Lorentzian oscillator model for Gallium Phosphide material. The particle swarm optimization approach is general so that other materials may be parameterized to the Lorentzian model and incorporated into time-domain modeling methods such as the finite-difference time-domain (FDTD).

Lord Rayleigh first investigated scattering from infinitely long dielectric cylinders in 1918. The analytical solution technique developed by Rayleigh was used to determine the electric fields inside and outside a long nanowire. A numeric code was developed to calculate the electric field magnitude inside and outside the wire

for a Gallium Phosphide nanowire excited at normal incidence by a transverse magnetic and transverse electric wave. The intensity integral was introduced for cylindrical geometry and applied to lossless and lossy dielectric nanowires for both transverse magnetic and transverse electric polarizations. It was determined that the transverse magnetic polarization is dominant for diameters below 125 nm. The polarization dependence at normal incidence was also investigated by deriving the internal electric intensity as a function the transverse magnetic and electric polarization intensities and the angle theta. For diameters where the transverse magnetic intensity dominates, it was determined the intensity has a dipole-like pattern. These properties agree with experimental data and discrete-dipole approximation calculations.

Surface impedance models are of great utility in electromagnetics because they provide an efficient method for representing the material and geometrical properties of a structure without the need for fine meshing. Surface impedance models for nanoslabs, nanowires and tubular nanowires were studied in this work. A surface impedance for a variable thickness slab surrounded by free-space was derived. It was shown that for slabs of large thickness, the surface impedance agrees with the surface impedance of a half-space. A vanishingly small slab was shown to have the surface impedance of free-space as expected. The surface impedance expression for a nanowire was examined and it was shown that for larger radii nanowires the surface impedance approaches that of a half-space. For the tubular nanowire, the surface impedance was derived using modal analysis and compared to an expression developed by King. It was determined that King's expression yields different results that predict different surface impedance values for small thickness tubular nanowires. Finally, a method of moments formulation for thin-wire dipole antennas was modified to incorporate a surface impedance model. Results comparing a perfectly conducting, gold, and silver nano-dipole show the importance of incorporating material properties at infrared and optical frequencies into the electromagnetic analysis of nanostructures. By developing modeling tools for nanowires, devices may be designed for optical detection and bio-sensing.

Table of Contents

List of Figures

List of Tables

Acknowledgments

There are several people who I would like to acknowledge for their assistance during my graduate studies. First and foremost, I would like to thank my advisor, Professor Douglas H. Werner. I would like to thank Professor Werner for his guidance and support during the duration of this research and for stimulating my interest in the field of electromagnetics and antennas as a young researcher. I would also like to thank Dr. Pingjuan L. Werner for serving as a member on my thesis committee. I would like to thank our collaborators, Professor Peter Elkund and his students and post-docs: Dr. Gugang Chen, Dr. Qihua Xiong, Dr. Humberto Gutirrez, Jian Wu and Qijue Lu for their help on the Gallium Phosphide nanowire research. I am grateful to have had the pleasure to work with many great labmates in the Computational Electromagnetics Research and Antennas Laboratory (CEARL) at Penn State. The present and past members of CEARL have provided me with many stimulating and fruitful discussions in the field of engineering and electromagnetics. Thanks is also due to the past and present members of Dr. Pasko's lab who have encouraged me during my graduate studies. I have met many amazing people during my time at Penn State and I would like to thank them all for their friendship. Finally, I want to thank my family for their continued love and support throughout my entire academic career.

Chapter 1

Introduction

1.1 Motivation

Current state-of-the-art fabrication techniques have made it possible to fabricate objects of diminishing size. These structures have enabled higher density integrated circuits to be designed. Applying these fabrication techniques to nanoscale metallic patches, nanowires and nanotubes, novel electromagnetic devices can be envisioned. In order to design novel infrared and optical devices, new modeling methods will have to be developed so that the properties of these structures can be understood. In the development of models for electromagnetic analysis of nanostructures, it is necessary to account for the behavior of materials at infrared and optical frequencies. We will discuss oscillator models for describing the dielectric properties of metals and semiconductors in the infrared and optical spectrum. These models will be applied to the study of nanoscale wires known as nanowires. Based on the solutions to the scattering from an infinitely long dielectric cylinder, the electric fields inside a nanowire will be calculated. The electromagnetic intensity inside the wire will be defined and calculated to show the diameter and polarization dependence of semiconducting nanowires. Surface impedance models for nanoslabs, nanowires and tubular nanowires will be derived for nanoslabs, nanowires and tubular nanowires. These models will allow for efficient computation of nanoscale electromagnetic structures through the use of method of moment calculations. By exploring these analysis techniques and developing models for nanoscale devices, new devices such as optical antennas and infrared frequency se-

lective surfaces (FSS) can be designed and optimized for applications in biosensing, energy harvesting and infrared/optical metamaterials.

1.2 Literature Review

We will begin our development of models for studying nanowires by providing an overview of recent work in the area of studying nanoscale electromagnetic devices. Current research of nanoscale structures is focused on high-aspect ratio structures such as nanoslabs, nanowires and nanotubes. Several methods have been developed to realize nanostructures during the past 10 years. Closely spaced metallic patches (nanoslabs), have also been fabricated at the micron and nanometer scale using contact lithography and electron-beam lithography [1, 2]. Synthesis of large arrays of carbon nanotubes have been demonstrated using a plasma-enhanced chemical vapor deposition (PECVD) process [3]. Growth of nanowires is performed using either vapor-liquid-solid (VLS) synthesis or template-assisted synthesis. The VLS synthesis technique is mainly used for semiconducting wires while the template-based synthesis technique may be used for metal nanowires [4, 5].

Optical properties of multi-walled carbon nanotubes (MWCNTs) were studied in [6]. Wang et. al. measured the reflected light intensity from random arrays of aligned carbon nanotubes. Based on their experimental measurements, a polarization effect and length effect were demonstrated. The polarization effect demonstrated shows that reflected light was suppressed when the incident electric field polarization was perpendicular to the nanotube axis while the length of the nanotubes impacted the wavelength at which the reflected light was maximum. Based on these experimental observations, Wang concluded that the random arrays of carbon nanotubes have an analogous behavior to that of conventional dipole antennas operating at radio frequencies [6]. The antenna properties of carbon nanotubes have been studied in more detail by Hanson [7, 8, 9, 10]. In [7], the input impedance of a single-wall carbon nanotube (SWNT) is determined and the efficiency calculated. Hanson utilizes the moment method and a surface impedance model for the nanotube dipole. Carbon nanotube dipoles of lengths $L = 1$ μm, 10 μm and 1 mm with dipole radius $a = 2.712$ nm were simulated at microwave and infrared

frequencies. Based on Hanson's calculations, the efficiency e_r is on the order of 10^{-5} to 10^{-6} [7]. Similar results for input impedance and efficiency were found by Burke et. al. Burke and co-authors used a transmission line model was developed for a carbon nanotube dipole where the resistance, inductance and capacitance along the line were determined by the geometry and nanotube material parameters. The effect of objects near nanotube antennas is also of practical interest [11]. In [10], a resonant nanosphere was placed near a long carbon nanotube and the current along the carbon nanotube was calculated. It was determined that placing a nanosphere near the carbon nanotube significantly effects the current along the carbon nanotube, but the backscattered electric field due to the carbon nanotube and nanosphere is mainly attributed to the presence of the nanosphere [10].

Electromagnetic modeling of nanowires has been investigated using finite-difference time-domain (FDTD), discrete-dipole approximation (DDA) and method of moment (MoM) techniques [12, 13, 14]. The absorption and scattering of an array of silver nanowires is investigated using FDTD and a Drude model to represent the dispersive material properties of silver at optical frequencies in [12]. Podolskiy et. al. investigated silver nanowire systems using DDA. Based on their calculations, nanowire systems were able to achieve simultaneously a negative permittivity and permeability, hence generating a negative-index metamaterial. Their DDA model also showed strong coupling between parallel wires allowing for light to propagate in the array with strong field enhancements which may be used for spectroscopy or lithography [14]. Silver nanowire resonators were studied in [15]. These silver nanowire resonators were studied experimentally at optical wavelengths and also show strong field enhancement at the nanowire tip [15]. A method of moment approach using a surface impedance model to incorporate material parameters was used by Hanson to study copper dipoles at infrared and optical frequencies. The efficiencies reported by Hanson are significantly higher than those of carbon nanotube dipoles and are on the order of 0.1 to 0.9 for nanowire radii varying from 10 nm to 60 nm at 396 THz [13]. A similar approach to the Hanson's will be used in Chapter 4 to calculate the input impedance of gold and silver nano-dipole antennas. Raman scattering from semiconducting nanowires has been studied in [16, 17, 18, 19] and will be discussed in greater detail in Chapter 2. Finally, a

gold-nano-particle embedded nanowire was recently demonstrated by Hu and co-authors which may be used as a nanoscale waveguide for optoelectronics [20].

Electron-beam fabrication techniques have also been used to fabricate planar optical antennas at the nanometer scale. These nano-scale optical antennas have been shown experimentally to have resonant behavior associated with their physical length [21, 22]. Chains of nanoholes fabricated in thin metallic films also exhibit dipole-like behavior [23]. Planar nanoslabs have recently been coupled to diodes. Using log-periodic and spiral antennas scaled to operate at the infrared, novel infrared detectors have been designed, fabricated and tested for room-temperature operation [24, 25]. Modeling tools have been used to optimize planar structures for infrared filter designs. This approach utilizes the genetic algorithm combined with nano-fabrication constraints in order to generate realizable designs [1, 2].

1.3 Material Models

Materials in the infrared and optical region are dispersive. In order to accurately calculate the field values of nanostructures at infrared and optical frequencies, the material behavior must be included in the model. In particular, metals in the infrared and optical spectrum do not exhibit the same behavior as in the RF and microwave region. Metals in the infrared and optical region exhibit a negative real part of the dielectric function. The real and imaginary part of metals at infrared and optical frequencies also vary over several orders of magnitude. Measured values for several metals were reported in the literature in the early 1970s [26]. Infrared and optical material properties of semiconductors have also been experimentally measured and reported in the literature [27, 28]. The experimental values were reported in terms of a complex refractive index ie. $\widehat{n} = n - jk$. The relations relating the real and imaginary ($\widehat{\epsilon}_r = \epsilon'_r - j\epsilon''_r$) components of the relative permittivity to the real and imaginary components of the refractive index as a function of radial frequency are given by:

$$\epsilon'_r(\omega) = n^2(\omega) - k^2(\omega) \tag{1.1}$$

$$\epsilon_r''(\omega) = 2n(\omega)k(\omega) \tag{1.2}$$

Similarly, the complex refractive can be expressed in terms of the complex permittivity:

$$n(\omega) = \frac{1}{\sqrt{2}}\left[\left(\left(\epsilon_r'(\omega)\right)^2 + \left(\epsilon_r''(\omega)\right)^2\right)^{\frac{1}{2}} + \epsilon_r'(\omega)\right]^{\frac{1}{2}} \tag{1.3}$$

$$k(\omega) = \frac{1}{\sqrt{2}}\left[\left(\left(\epsilon_r'(\omega)\right)^2 + \left(\epsilon_r''(\omega)\right)^2\right)^{\frac{1}{2}} - \epsilon_r'(\omega)\right]^{\frac{1}{2}} \tag{1.4}$$

As can be seen above, the convention for describing materials in the infrared and optical spectrum is to use the complex permittivity instead of the conductivity of a material. The convention used in the RF is to describe the property of a material by its real permittivity and conductivity as shown in equation (1.5) where the DC conductivity is scaled by the radial frequency ω.

$$\widehat{\epsilon}(\omega) = \epsilon'(\omega) - j\frac{\sigma}{\epsilon_0\omega} \tag{1.5}$$

In the following sections, we will present oscillator models used to describe the complex permittivity of real materials. These models are convenient repesentations of the dielectric function. In addition, oscillator models are useful for implementing dispersive materials in finite-difference time-domain (FDTD) codes [29]. The Lorentz-Drude oscillator model for complex permittivity will be introduced. The Particle Swarm Optimization (PSO) algorithm will also be applied to optimizing parameters of a Lorentzian oscillator model for a semiconducting material.

1.3.1 Lorentz-Drude Model

A convenient method to parameterize a complex dielectric function is to use damped harmonic oscillators. These models were constructed to represent the frequency dependence of material characteristics . Two well-known oscillator models are the Drude model and Lorentzian model. The Drude model may be used to described the intraband effects while the Lorentzian oscillator is used to describe interband effects. The Lorentz-Drude model is a superposition of a Drude model

with the Lorentzian oscillators model as shown in equation (1.6).

$$\widehat{\epsilon}_r(\omega) = \widehat{\epsilon}_{r_{(Drude)}}(\omega) + \widehat{\epsilon}_{r_{(Lorentz)}}(\omega) \tag{1.6}$$

where the Drude and Lorentz portions of the complex permittivity are shown in equations (1.7) and (1.8)

$$\widehat{\epsilon}_{r_{(Drude)}}(\omega) = 1 - \frac{\Omega_p^2}{\omega\big(\omega - j\Gamma_0\big)} \tag{1.7}$$

$$\widehat{\epsilon}_{r_{(Lorentz)}}(\omega) = \sum_{n=1}^{N} \frac{f_n\omega_p^2}{\big(\omega_n^2 - \omega^2\big) + j\omega\Gamma_n} \tag{1.8}$$

where ω_p is the plasma frequency, N is the number of oscillators with frequency ω_n, strength f_n, lifetime $1/\Gamma_n$, plasma frequency $\Omega_p = \sqrt{f_0}\omega_p$, oscillator strength f_0 and damping constant Γ_0. The parameters for several common metals such as Silver (Ag), Gold (Au), Copper (Cu), and Aluminum (Al) have been published in [30]. The dielectric function for Gold and Silver based on the Lorentz-Drude model parameters from the Rakic el. al were calculated and shown in Figure 1.1.

1.3.2 Particle Swarm Optimization for Parameter Fitting Lorentzian Models

Swarm intelligence is a nature-based stochastic optimization technique which was introduced by James Kennedy and Russel C. Eberhart [31]. Kennedy and Eberhart studied the behavior of animals in their groups, swarms, or schools. Based on their studies, they parameterized core operators for the Particle Swarm Optimization (PSO) algorithm. The goal of the PSO algorithm is to imitate the success of individuals in optimization as a group. The Particle Swarm Optimization technique is a relatively simple, but flexible and robust optimization algorithm which can be applied to many engineering problems where the problem can be multi-dimensional, multi-objective, real-valued or discrete-valued. The algorithm also allows additional restrictions to be set as required. Figure 1.2 illustrates the operation of the PSO algorithm. An initial population is created and the fitness is evaluated. Based on the fitness of the particle, the particle is evaluated to deter-

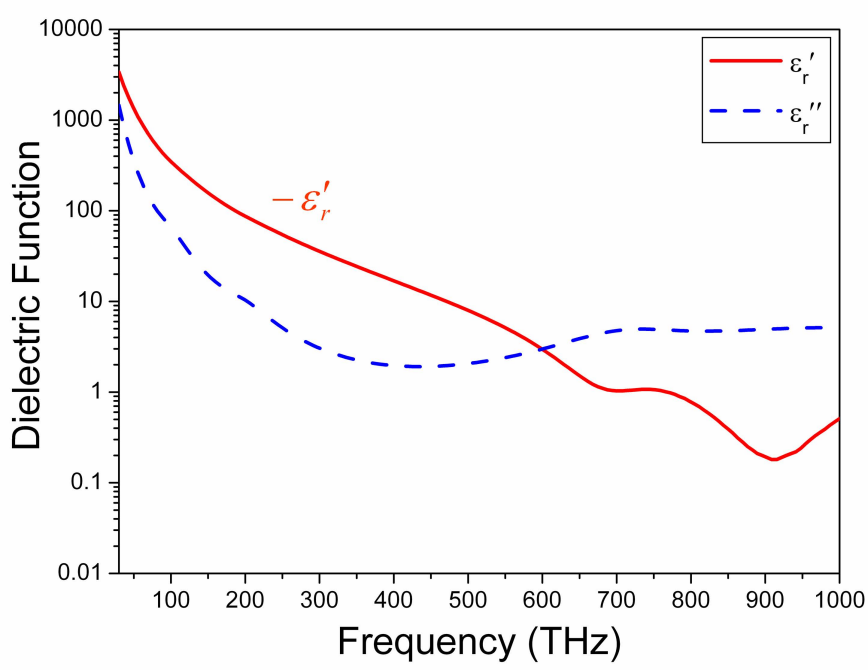

(a) Gold (Au) dielectric function

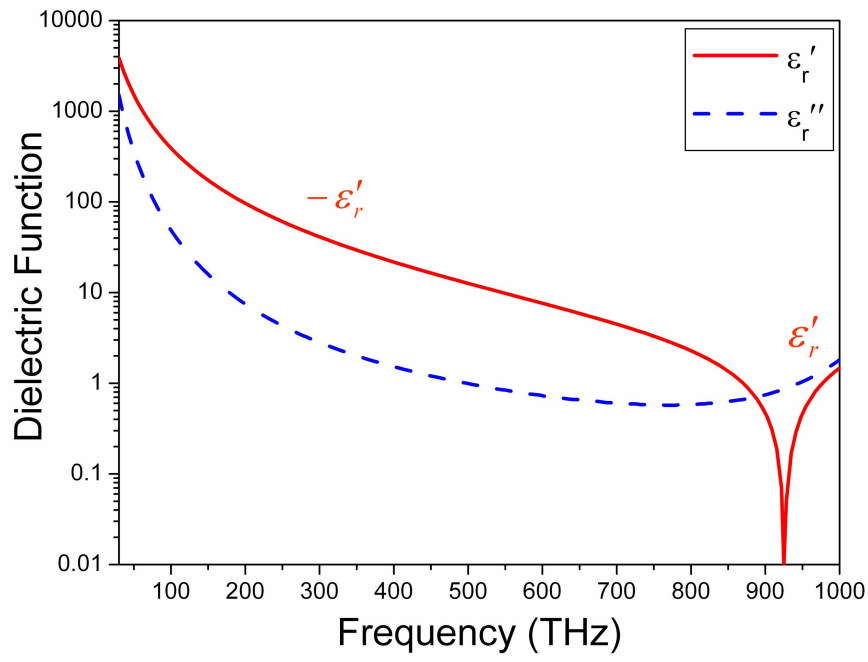

(b) Silver (Ag) dielectric function

Figure 1.1: Dielectric functions of Gold and Silver calculated from Lorentz-Drude models.

mine if it meets the criteria for personal best and global best. Particle velocities and positions are then updated and the sequence occurs again until the global optimum is achieved or the maximum number of iterations is reached. The parti-

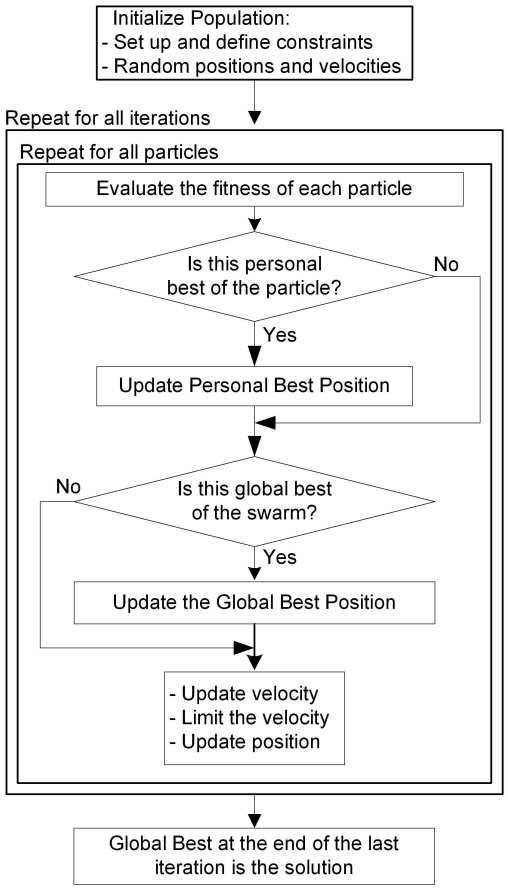

Figure 1.2: Particle Swarm Optimization (PSO) algorithm flowchart

cle swarm optimization algorithm has been used in electromagnetics to implement the design of Yagi-Uda arrays and conformal array excitation amplitude synthesis [32, 33]. The PSO technique has also been developed to optimize parameter values for Debye functions [34]. Similar to the the Lorentz-Drude oscillator model, the Debye function can be used to represent frequency dependent dielectric functions. We will use a Lorentzian oscillator model of the form shown in equation (1.9) to represent the complex dielectric function of a semiconducting material. The model parameters are ϵ_∞ (the high frequency permittivity), N (number of oscillators in the model), ϵ_{sn} (low frequency permittivity for the nth oscillator), $\omega_{o\epsilon n}$ (resonance

frequency for the nth oscillator), and $\delta_{\epsilon n}$ (the damping factor for the nth oscillator).

$$\widehat{\epsilon}_r(\omega) = \epsilon_\infty + \sum_{n=1}^{N} \frac{\left(\epsilon_{sn} - \epsilon_\infty\right)\omega_{o\epsilon n}^2}{\omega_{o\epsilon n}^2 + j2\delta_{\epsilon n}\omega - \omega^2} \tag{1.9}$$

A Lorentzian model was developed for the semiconductor Gallium Phosphide (GaP) at infrared and optical frequencies using a PSO algorithm with the number of oscillators being fixed at 8. Experimental values for the GaP material at optical frequencies were taken from [27, 28]. The fitness function used for the optimization is shown in equation (1.10) and was minimized over the frequency range from 10 THz to 10000 THz. Figure 1.3 shows that the PSO determined Lorentzian model parameter fit agrees well with the experimental data.

$$f = \sum |\widehat{\epsilon}_{r_{(PSO)}}(\omega) - \widehat{\epsilon}_{r_{(Experimental)}}(\omega)|^2 \tag{1.10}$$

1.4 Summary

Novel fabrication techniques of nanometer scale structures have been discussed in the literature. These fabrication techniques have been used to create nanoslabs, nanowires and nanotubes. In order to understand the behavior of these structures, the dispersive nature of the materials must be incorporated into the modeling method. The Lorentz-Drude and Lorentzian oscillator models were presented for metallic and semiconducting materials in the infrared and optical spectrum. A particle swarm optimization technique was used to parameter fit a semiconducting material to a Lorentzian oscillator model. The PSO technique is a general technique that can be used to generate an oscillator model for other materials given the measured dielectric function. The electric fields inside nanowires will now be investigated by solving the classical scattering from infinitely long dielectric nanowires and calculating the internal electric field intensity.

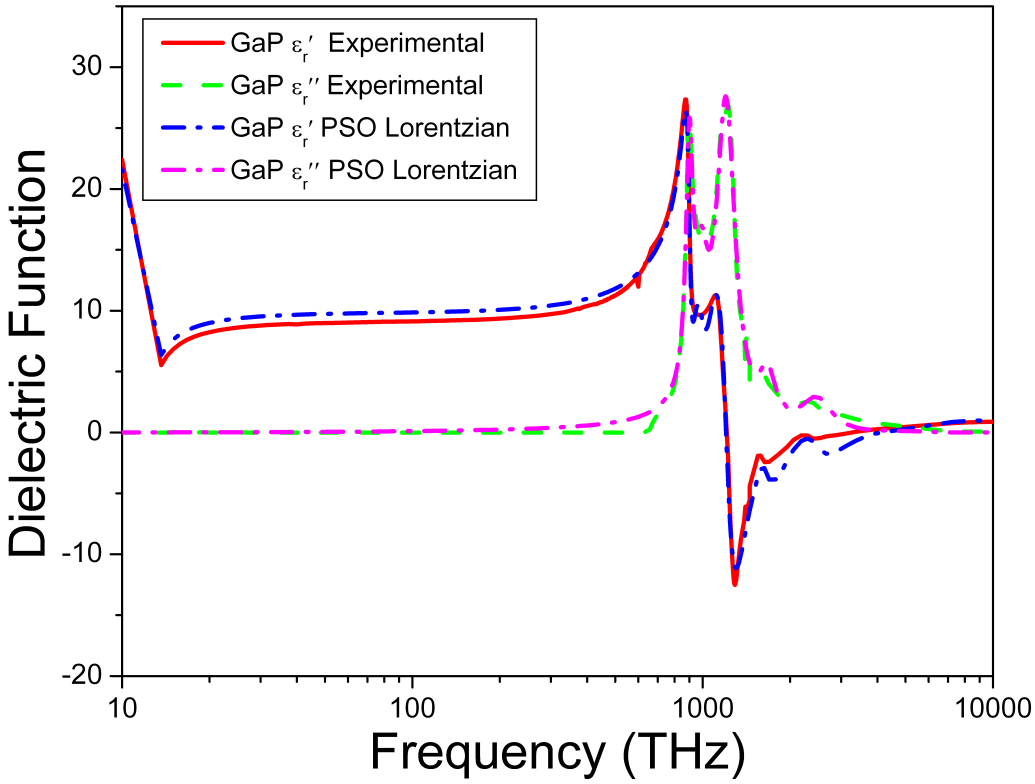

Figure 1.3: Comparison of experimental GaP data and PSO Lorentzian model for GaP.

Chapter 2

Internal Electromagnetic Intensity of Dielectric Nanowires

2.1 Introduction

In this chapter we will examine the enhanced electric fields that develop inside nanowires due to resonances that occur inside the wire. We will first begin by applying analytical tools to study dielectric nanowires. Under the assumption that the nanowire is long, an infinite cylinder may be used to examine the electric fields inside the nanowire. Defining an intensity integral for the fields inside the wire we may also determine the internal electromagnetic field intensity inside the nanowire as a function of its diameter and material properties. The internal electromagnetic field intensity integral can then be used to examine the resonant properties of long nanowires. The internal electromagnetic intensity will be calculated for a Gallium Phosphide nanowire in the optical spectrum. A method for examing the polarization dependence at normal incidence of the internal electromagnetic intensity will be applied to nanowires.

2.2 Scattering from Infinite Dielectric Cylinders

The derivation of scattering at normal incidence from an infinitely long dielectric cylinder was first published by Lord Rayleigh in 1918 [35]. Rayleigh's derivation

has been re-examined several times in the literature [36, 37, 38]. Scattering at oblique incidence from an infinitely long dielectric cylinder has been examined by Wait in [39]. In this section, the derivation from scattering from an infinitely long dielectric cylinder at normal incidence will be re-examined for the transverse magnetic and transverse electric polarizations. Based on these closed-form solutions, calculations for the electric field magnitudes inside and outside the wire will be shown for varying cylinder diameters using the dielectric properties of a semiconducting material.

2.2.1 Transverse Magnetic (TM^z) Polarization

The transverse magnetic (TM^z) polarization will be examined first. The dielectric cylinder axis is in the $\hat{z}$ direction as shown in Figure 2.1.

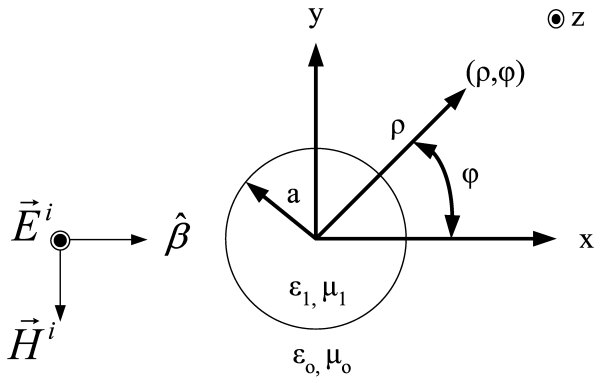

Figure 2.1: Geometry for the TM^z polarization.

For this geometry the electric fields inside and outside the wire are $\hat{z}$-directed and can be represented as an infinite summation of cylindrical harmonics shown below:

$$\vec{E}_i^{TM} = \hat{a_z} E_0 \sum_{n=-\infty}^{+\infty} j^{-n} J_n(\beta_0 \rho) e^{jn\phi} \tag{2.1}$$

$$\vec{E}_s^{TM} = \hat{a_z} E_0 \sum_{n=-\infty}^{+\infty} a_n^{TM} H_n^{(2)}(\beta_0 \rho) e^{jn\phi} \tag{2.2}$$

$$\vec{E}_d^{TM} = \hat{a_z} E_0 \sum_{n=-\infty}^{+\infty} \left[b_n^{TM} J_n(\beta_1 \rho) + c_n^{TM} Y_n(\beta_1 \rho) \right] e^{jn\phi} \tag{2.3}$$

where

$$\beta_0 = \omega\sqrt{\mu_0\epsilon_0} \tag{2.4}$$

$$\beta_1 = \omega\sqrt{\mu_1\epsilon_1} \tag{2.5}$$

The incident, scattered and transmitted magnetic fields can be obtained from Maxwell's equations:

$$\vec{H} = -\frac{1}{j\omega\mu}\nabla\times\vec{E} = -\frac{1}{j\omega\mu}\left[\hat{a_\rho}\frac{1}{\rho}\frac{\partial E_z}{\partial\phi} - \hat{a_\phi}\frac{\partial E_z}{\partial\rho}\right] \tag{2.6}$$

Yielding the following expressions for the magnetic fields:

$$\vec{H}_i^{TM} = -\hat{a_\rho}\frac{E_0}{j\omega\mu_0}\frac{1}{\rho}\sum_{n=-\infty}^{+\infty} nj^{-n+1}J_n(\beta_0\rho)e^{jn\phi} + \hat{a_\phi}\frac{E_0\beta_0}{j\omega\mu_0}\sum_{n=-\infty}^{+\infty} j^{-n}J_n'(\beta_0\rho)e^{jn\phi} \tag{2.7}$$

$$\vec{H}_s^{TM} = -\hat{a_\rho}\frac{E_0}{j\omega\mu_0}\frac{1}{\rho}\sum_{n=-\infty}^{+\infty} (jn)a_n^{TM}H_n^{(2)}(\beta_0\rho)e^{jn\phi} + \hat{a_\phi}\frac{E_0\beta_0}{j\omega\mu_0}\sum_{n=-\infty}^{+\infty} a_n^{TM}H_n^{(2)'}(\beta_0\rho)e^{jn\phi} \tag{2.8}$$

$$\begin{aligned}\vec{H}_d^{TM} = -\hat{a_\rho}\frac{E_0}{j\omega\mu_1}\frac{1}{\rho}\sum_{n=-\infty}^{+\infty} (jn)\left[b_n^{TM}J_n(\beta_1\rho) + c_n^{TM}Y_n(\beta_1\rho)\right]e^{jn\phi} \\ +\hat{a_\phi}\frac{E_0\beta_1}{j\omega\mu_1}\sum_{n=-\infty}^{+\infty}\left[b_n^{TM}J_n'(\beta_1\rho) + c_n^{TM}Y_n'(\beta_1\rho)\right]e^{jn\phi}\end{aligned} \tag{2.9}$$

where

$$' = \frac{\partial}{\partial(\beta\rho)} \tag{2.10}$$

The coefficients a_n^{TM}, b_n^{TM} and c_n^{TM} can be solved by applying boundary conditions are the interface between the two materials $\rho = a$. Physically, the fields everywhere must be finite everywhere, therefore, c_n^{TM} must be zero due to the Bessel function of the second kind having a singularity for $\beta\rho = 0$. Assuming the materials are non-magnetic ($\mu_1 = \mu_0$), the following two equations relate a_n^{TM} and b_n^{TM}.

$$j^{-n}J_n(\beta_0 a) + a_n^{TM}H_n^{(2)}(\beta_0 a) = b_n^{TM}J_n(\beta_1 a) \tag{2.11}$$

$$j^{-n}J_n'(\beta_0 a) + a_n^{TM}H_n^{(2)'}(\beta_0 a) = \sqrt{\epsilon_{r1}}b_n^{TM}J_n'(\beta_1 a) \tag{2.12}$$

Expressions for a_n^{TM}, b_n^{TM} and c_n^{TM} can be obtained from the above equations and are shown below. The relative permittivity within the cylinder is defined as ϵ_{r1}.

$$a_n^{TM} = j^{-n} \frac{J_n'(\beta_0 a) J_n(\beta_1 a) - \sqrt{\epsilon_{r1}} J_n(\beta_0 a) J_n'(\beta_1 a)}{\sqrt{\epsilon_{r1}} J_n'(\beta_1 a) H_n^{(2)}(\beta_0 a) - J_n(\beta_1 a) H_n^{(2)'}(\beta_0 a)} \tag{2.13}$$

$$b_n^{TM} = j^{-n} \frac{J_n(\beta_0 a) H_n^{(2)'}(\beta_0 a) - J_n'(\beta_0 a) H_n^{(2)}(\beta_0 a)}{J_n(\beta_1 a) H_n^{(2)'}(\beta_0 a) - \sqrt{\epsilon_{r1}} J_n'(\beta_1 a) H_n^{(2)}(\beta_0 a)} \tag{2.14}$$

$$c_n^{TM} = 0 \tag{2.15}$$

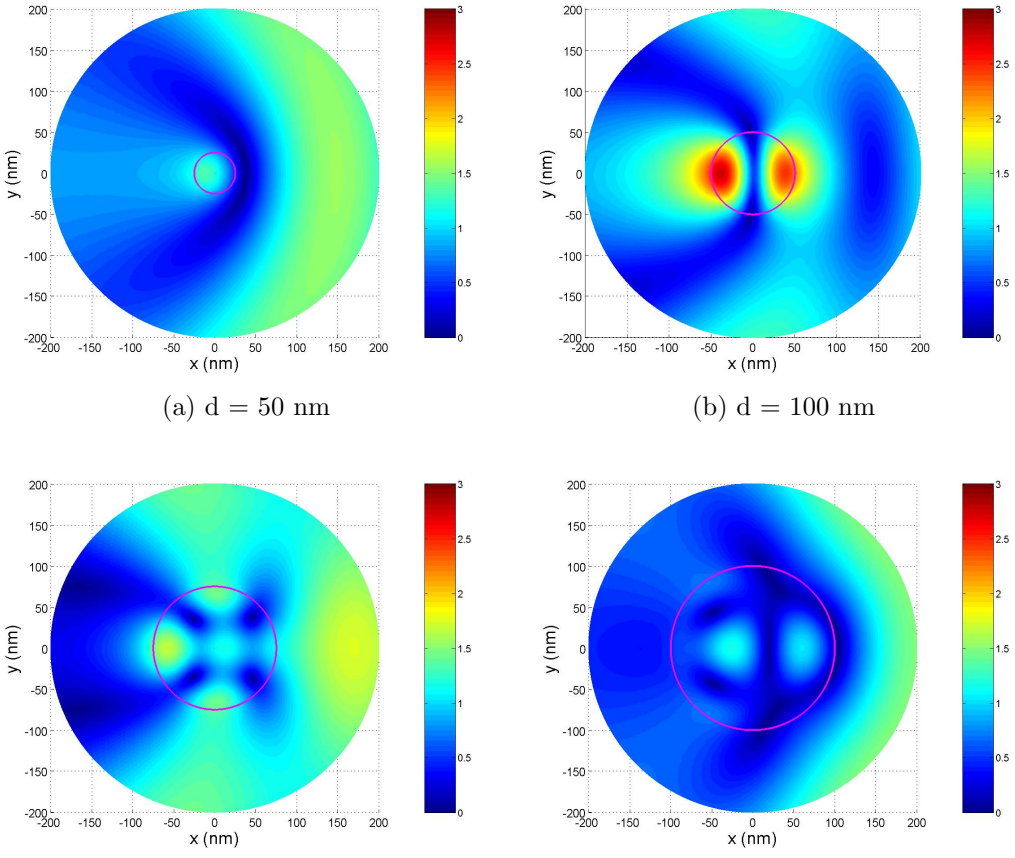

(a) d = 50 nm

(b) d = 100 nm

(c) d = 150 nm

(d) d = 200 nm

Figure 2.2: Electric field magnitude plots for TM^z polarization incident wave on a Gallium Phosphide nanowire excited at $\lambda = 488$ nm.

A computer program in MATLAB was developed to calculate the electric field

magnitude inside and outside a GaP nanowire shown in Figure 2.2. The code calculates the necessary Bessel and Hankel functions and their derivatives. Since the fields are represented by an infinite series, the summation must be truncated after N number of terms. It determined that taking the first 30 terms was sufficient for convergence of the infinite series. The incident wave was TM^z polarized and traveling in the $+\hat{x}$ direction with $E_0 = 1$. The excitation wavelength chosen was $\lambda = 488$ nm. At this wavelength the permittivity of GaP is $\epsilon_{r1} = 13.2382 - j0.0003$. It can be seen in Figure 2.2, that the electric field magnitude is continuous at the boundary between free-space and the nanowire since only tangential $\hat{z}$ directed fields are present in the TM^z polarization.

2.2.2 Transverse Electric (TE^z) Polarization

The transverse electric (TE^z) polarization assumes the magnetic fields inside and outside the wire are $\hat{z}$-directed. The geometry for the TE^z polarization is shown in Figure 2.3.

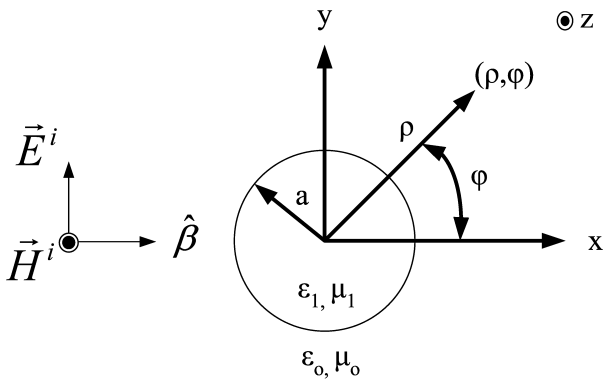

Figure 2.3: Geometry for the TE^z polarization.

An infinite summation of cylindrical harmonics can also be used to represent the fields as shown in the following equations:

$$\vec{H}_i^{TE} = \hat{a_z} H_0 \sum_{n=-\infty}^{+\infty} j^{-n} J_n(\beta_0 \rho) e^{jn\phi} \tag{2.16}$$

$$\vec{H}_s^{TE} = \hat{a_z} H_0 \sum_{n=-\infty}^{+\infty} a_n^{TE} H_n^{(2)}(\beta_0 \rho) e^{jn\phi} \tag{2.17}$$

$$\vec{H}_d^{TE} = \hat{a_z} H_0 \sum_{n=-\infty}^{+\infty} \left[b_n^{TE} J_n(\beta_1 \rho) + c_n^{TE} Y_n(\beta_1 \rho) \right] e^{jn\phi} \tag{2.18}$$

The incident, scattered and transmitted electric fields are obtained from Maxwell's equations:

$$\vec{E} = -\frac{1}{j\omega\epsilon_0} \nabla \times \vec{H} = \frac{1}{j\omega\epsilon} \left[\hat{a_\rho} \frac{1}{\rho} \frac{\partial H_z}{\partial \phi} - \hat{a_\phi} \frac{\partial H_z}{\partial \rho} \right] \tag{2.19}$$

Yielding the following expressions for the magnetic fields:

$$\vec{E}_i^{TE} = \hat{a_\rho} \frac{H_0}{j\omega\epsilon_0} \frac{1}{\rho} \sum_{n=-\infty}^{+\infty} n j^{-n+1} J_n(\beta_0 \rho) e^{jn\phi} - \hat{a_\phi} \frac{H_0 \beta_0}{j\omega\epsilon_0} \sum_{n=-\infty}^{+\infty} j^{-n} J_n'(\beta_0 \rho) e^{jn\phi} \tag{2.20}$$

$$\vec{E}_s^{TE} = \hat{a_\rho} \frac{H_0}{j\omega\epsilon_0} \frac{1}{\rho} \sum_{n=-\infty}^{+\infty} (jn) a_n^{TE} H_n^{(2)}(\beta_0 \rho) e^{jn\phi} - \hat{a_\phi} \frac{H_0 \beta_0}{j\omega\epsilon_0} \sum_{n=-\infty}^{+\infty} a_n^{TE} H_n^{(2)'}(\beta_0 \rho) e^{jn\phi} \tag{2.21}$$

$$\begin{aligned} \vec{E}_d^{TE} = \hat{a_\rho} \frac{H_0}{j\omega\epsilon_1} \frac{1}{\rho} \sum_{n=-\infty}^{+\infty} (jn) \left[b_n^{TE} J_n(\beta_1 \rho) + c_n^{TE} Y_n(\beta_1 \rho) \right] e^{jn\phi} \\ - \hat{a_\phi} \frac{H_0 \beta_1}{j\omega\epsilon_1} \sum_{n=-\infty}^{+\infty} \left[b_n^{TE} J_n'(\beta_1 \rho) + c_n^{TE} Y_n'(\beta_1 \rho) \right] e^{jn\phi} \end{aligned} \tag{2.22}$$

The TE^z field incident field magnitude H_0 can be related to the incident electric field magnitude E_0 by the intrinsic impedance

$$\eta_0 = \frac{E_0}{H_0} = \sqrt{\frac{\mu_0}{\epsilon_0}} \tag{2.23}$$

hence

$$H_0 = \frac{E_0}{\eta_0} \tag{2.24}$$

Rewriting the magnetic and electric fields in terms of the incident electric field magnitude, we obtain the following expressions:

$$\vec{H}_i^{TE} = \hat{a_z} \frac{E_0}{\eta_0} \sum_{n=-\infty}^{+\infty} j^{-n} J_n(\beta_0 \rho) e^{jn\phi} \tag{2.25}$$

$$\vec{H}_s^{TE} = \hat{a_z}\frac{E_0}{\eta_0}\sum_{n=-\infty}^{+\infty} a_n^{TE} H_n^{(2)}(\beta_0\rho)e^{jn\phi} \tag{2.26}$$

$$\vec{H}_d^{TE} = \hat{a_z}\frac{E_0}{\eta_0}\sum_{n=-\infty}^{+\infty}\left[b_n^{TE} J_n(\beta_1\rho) + c_n^{TE} Y_n(\beta_1\rho)\right]e^{jn\phi} \tag{2.27}$$

$$\vec{E}_i^{TE} = \hat{a_\rho}\frac{E_0}{j\omega\epsilon_0\eta_0}\frac{1}{\rho}\sum_{n=-\infty}^{+\infty} nj^{-n+1} J_n(\beta_0\rho)e^{jn\phi} - \hat{a_\phi}\frac{E_0\beta_0}{j\omega\epsilon_0\eta_0}\sum_{n=-\infty}^{+\infty} j^{-n} J_n'(\beta_0\rho)e^{jn\phi} \tag{2.28}$$

$$\vec{E}_s^{TE} = \hat{a_\rho}\frac{E_0}{j\omega\epsilon_0\eta_0}\frac{1}{\rho}\sum_{n=-\infty}^{+\infty} (jn)a_n^{TE} H_n^{(2)}(\beta_0\rho)e^{jn\phi} - \hat{a_\phi}\frac{E_0\beta_0}{j\omega\epsilon_0\eta_0}\sum_{n=-\infty}^{+\infty} a_n^{TE} H_n^{(2)'}(\beta_0\rho)e^{jn\phi} \tag{2.29}$$

$$\begin{aligned}\vec{E}_d^{TE} = \hat{a_\rho}\frac{E_0}{j\omega\epsilon_1\eta_0}\frac{1}{\rho}\sum_{n=-\infty}^{+\infty} (jn)\left[b_n^{TE} J_n(\beta_1\rho) + c_n^{TE} Y_n(\beta_1\rho)\right]e^{jn\phi} \\ -\hat{a_\phi}\frac{\beta_1 E_0}{j\omega\epsilon_1\eta_0}\sum_{n=-\infty}^{+\infty}\left[b_n^{TE} J_n'(\beta_1\rho) + c_n^{TE} Y_n'(\beta_1\rho)\right]e^{jn\phi}\end{aligned} \tag{2.30}$$

The coefficient, c_n^{TE} must be zero due to the Bessel function of the second kind having a singularity for $\beta\rho = 0$. The two coefficients a_n^{TE} and b_n^{TE} can be determined by applying boundary conditions at the interface between the two materials $\rho = a$.

$$j^{-n} J_n(\beta_0 a) + a_n^{TE} H_n^{(2)}(\beta_0 a) = b_n^{TE} J_n(\beta_1 a) \tag{2.31}$$

$$j^{-n} J_n'(\beta_0 a) + a_n^{TE} H_n^{(2)'}(\beta_0 a) = \frac{1}{\sqrt{\epsilon_{r1}}} b_n^{TE} J_n'(\beta_1 a) \tag{2.32}$$

Solving the above two equations gives the following expressions for a_n^{TE} and b_n^{TE} assuming the materials are non-magnetic. The relative permittivity for the dielectric material inside the cylinder is represented by ϵ_{r1}.

$$a_n^{TE} = j^{-n}\frac{J_n'(\beta_0 a)J_n(\beta_1 a) - \frac{1}{\sqrt{\epsilon_{r1}}} J_n(\beta_0 a)J_n'(\beta_1 a)}{\frac{1}{\sqrt{\epsilon_{r1}}} J_n'(\beta_1 a)H_n^{(2)}(\beta_0 a) - J_n(\beta_1 a)H_n^{(2)'}(\beta_0 a)} \tag{2.33}$$

$$b_n^{TE} = j^{-n}\frac{J_n(\beta_0 a)H_n^{(2)'}(\beta_0 a) - J_n'(\beta_0 a)H_n^{(2)}(\beta_0 a)}{J_n(\beta_1 a)H_n^{(2)'}(\beta_0 a) - \frac{1}{\sqrt{\epsilon_{r1}}} J_n'(\beta_1 a)H_n^{(2)}(\beta_0 a)} \tag{2.34}$$

$$c_n^{TE} = 0 \tag{2.35}$$

A computer code was used to calculate the electric field magnitude due to a

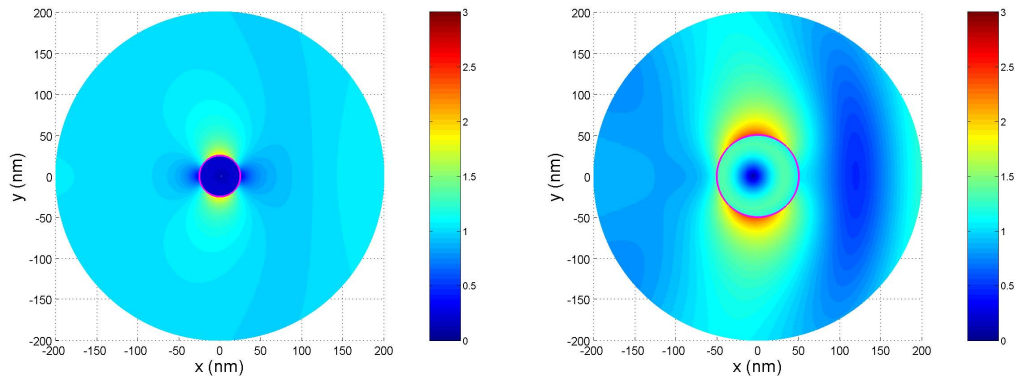

(a) d = 50 nm (b) d = 100 nm

(c) d = 150 nm (d) d = 200 nm

Figure 2.4: Electric field magnitude plots for TE^z polarization incident wave on a Gallium Phosphide nanowire excited at $\lambda = 488$ nm.

transverse electric incident wave propagating in the $+\hat{x}$ direction upon a GaP nanowire shown in Figure 2.4 with $E_0 = 1$. The infinite summation was truncated after 30 terms which provided sufficient convergence. The excitation wavelength chosen was $\lambda = 488$ nm with permittivity of GaP equal to $\epsilon_{r1} = 13.2382 - j0.0003$ at this wavelength. In Figure 2.4, it should be noted that the electric field magnitude is discontinuous at the boundary between free-space and the GaP nanowire due to the TE^z polarization containing both $\hat{\rho}$ and $\hat{\phi}$ directed components.

2.3 The Internal Electromagnetic Intensity Integral

Resonances of cylindrical dielectric wires are known to have enhanced internal electric fields [40]. In order to study the enhanced internal electric field inside cylinders, it was first proposed by Ruppin to use an internal electromagnetic field intensity integral. The intensity integral may be used to examine resonances associated with the size and material properties of the cylinder and is shown below in equation (2.36) [41].

$$I = \frac{1}{\pi a^2} \int_0^a \int_0^{2\pi} |\vec{E}|^2 \rho d\rho d\phi \tag{2.36}$$

The intensity integral has been recently used to the study of nanowires by Cao and co-authors. Cao used the internal electromagnetic intensity integral to study the Raman enhancement of Silicon nanowires [16]. In Cao's paper, only the lossless case for the intensity integral is discussed for the two normal incidence polarizations. Solutions for the intensity integral will be calculated in the following sections for the case where the material has purely real dielectric function (lossless) and also for the case when the material has a complex permittivity (lossy). These solutions will then be applied to the study of Gallium Phosphide nanowires.

2.3.1 Closed-form Solution for Lossless Case

2.3.1.1 Solution for TM^z Polarization

We first examine the TM^z case for a lossless medium. For the lossless case, we apply the following integral:

$$I_{TM} = \frac{1}{\pi a^2} \int_0^a \int_0^{2\pi} |\vec{E}_d^{TM}|^2 \rho d\rho d\phi \tag{2.37}$$

In order to calculate the intensity, the magnitude of the electric field inside the wire must be calculated.

$$|\vec{E}_d^{TM}|^2 = |E_0|^2 \left| \sum_{n=-\infty}^{+\infty} b_n^{TM} J_n(\beta_1 \rho) e^{jn\phi} \right|^2 \tag{2.38}$$

$$|\vec{E}_d^{TM}|^2 = |E_0|^2 \sum_{n=-\infty}^{+\infty} b_n^{TM} J_n(\beta_1\rho) e^{jn\phi} \sum_{n=-\infty}^{+\infty} b_n^{TM*} J_n^*(\beta_1\rho) e^{-jn\phi} \tag{2.39}$$

$$|\vec{E}_d^{TM}|^2 = |E_0|^2 \sum_{n=-\infty}^{+\infty} \sum_{m=-\infty}^{+\infty} b_n^{TM} b_m^{TM*} J_n(\beta_1\rho) J_m^*(\beta_1\rho) e^{j(n-m)\phi} \tag{2.40}$$

but $J_n^*(\beta_1\rho) = J_n(\beta_1^*\rho)$ for $\beta_1 \in \mathbb{C}$ and $\rho \in \mathbb{R}$. Since $\beta_1 = \beta_1^*$ for lossless material (ie. $\beta_1 \in \mathbb{R}$), then $J_n^*(\beta_1\rho) = J_n(\beta_1\rho)$ and equation (2.32) becomes

$$|\vec{E}_d^{TM}|^2 = |E_0|^2 \sum_{n=-\infty}^{+\infty} \sum_{m=-\infty}^{+\infty} b_n^{TM} b_m^{TM*} J_n(\beta_1\rho) J_m(\beta_1\rho) e^{j(n-m)\phi} \tag{2.41}$$

Substituting equation (2.33) into equation (2.30), we obtain

$$I_{TM} = \frac{1}{\pi a^2} |E_0|^2 \sum_{n=-\infty}^{+\infty} \sum_{m=-\infty}^{+\infty} \int_0^{2\pi} e^{j(n-m)\phi} d\phi \int_0^a \rho J_n(\beta_1\rho) J_m(\beta_1\rho) d\rho \tag{2.42}$$

but we know that

$$\int_0^{2\pi} e^{j(n-m)\phi} d\phi = \begin{cases} 2\pi & n = m \\ 0 & n \neq m \end{cases} \tag{2.43}$$

thus,

$$I_{TM} = \frac{2}{a^2} |E_0|^2 \sum_{n=-\infty}^{+\infty} |b_n^{TM}|^2 \int_0^a \rho J_n^2(\beta_1\rho) d\rho \tag{2.44}$$

Using the following integral found in [42]:

$$\int_0^a \rho J_n^2(\beta_1\rho) d\rho = \frac{a^2}{2} \left[J_n(\beta_1 a) - J_{n-1}(\beta_1 a) J_{n+1}(\beta_1 a) \right] \tag{2.45}$$

Hence, the closed-form solution for the intensity integral for the lossless TM^z case is

$$I_{TM} = |E_0|^2 \sum_{n=-\infty}^{+\infty} |b_n^{TM}|^2 \left[J_n^2(\beta_1 a) - J_{n-1}(\beta_1 a) J_{n+1}(\beta_1 a) \right] \tag{2.46}$$

2.3.1.2 Solution for TE^z Polarization

For the TE^z case, we apply a similar integral shown below to determine the internal electric field intensity. In this case, the form for the internal electric field for the

TE^z case is given by equation (2.22)

$$I_{TE} = \frac{1}{\pi a^2} \int_0^a \int_0^{2\pi} |\vec{E}_d^{TE}|^2 \rho d\rho d\phi \tag{2.47}$$

The magnitude of the internal electric field must be calculated. Since there are both $\hat{\rho}$ and $\hat{\phi}$ components, the magnitude squared is given by:

$$|\vec{E}_d^{TE}|^2 = |\vec{E}_{d\rho}^{TE}|^2 + |\vec{E}_{d\phi}^{TE}|^2 \tag{2.48}$$

Substituting equation (2.48) into (2.47), we obtain

$$I_{TE} = \frac{1}{\pi a^2} \int_0^a \int_0^{2\pi} \left\{ |\vec{E}_{d\rho}^{TE}|^2 + |\vec{E}_{d\phi}^{TE}|^2 \right\} \rho d\rho d\phi \tag{2.49}$$

Next, we calculate the magnitudes for each of the components

$$\begin{aligned} |\vec{E}_{d\rho}^{TE}|^2 &= \frac{|E_0|^2}{\omega^2 \epsilon_1 \epsilon_1^* \eta_0^2} \frac{1}{\rho^2} \sum_{n=-\infty}^{+\infty} (jn) b_n^{TE} J_n(\beta_1 \rho) e^{jn\phi} \sum_{n=-\infty}^{+\infty} (-jn) b_n^{TE*} J_n^*(\beta_1 \rho) e^{-jn\phi} \\ &= \frac{|E_0|^2}{\omega^2 \epsilon_1 \epsilon_1^* \eta_0^2} \frac{1}{\rho^2} \sum_{n=-\infty}^{+\infty} \sum_{m=-\infty}^{+\infty} (nm) b_n^{TE} b_m^{TE*} J_n(\beta_1 \rho) J_m^*(\beta_1 \rho) e^{j(n-m)\phi} \end{aligned} \tag{2.50}$$

$$\begin{aligned} |\vec{E}_{d\phi}^{TE}|^2 &= \frac{|E_0|^2 \beta_1 \beta_1^*}{\omega^2 \epsilon_1 \epsilon_1^* \eta_0^2} \sum_{n=-\infty}^{+\infty} b_n^{TE} J_n'(\beta_1 \rho) e^{jn\phi} \sum_{n=-\infty}^{+\infty} b_n^{TE*} J_n'^*(\beta_1 \rho) e^{-jn\phi} \\ &= \frac{|E_0|^2 \beta_1 \beta_1^*}{\omega^2 \epsilon_1 \epsilon_1^* \eta_0^2} \sum_{n=-\infty}^{+\infty} \sum_{m=-\infty}^{+\infty} b_n^{TE} b_m^{TE*} J_n'(\beta_1 \rho) J_m'^*(\beta_1 \rho) e^{j(n-m)\phi} \end{aligned} \tag{2.51}$$

but for lossless materials there is no imaginary part of the permittivity, hence $\epsilon_1 \in \mathbb{R}$ and $\beta_1 \in \mathbb{R}$ which implies $\epsilon_1^* = \epsilon_1$ and $\beta_1^* = \beta_1$. The above equations can then be simplified to

$$|\vec{E}_{d\rho}^{TE}|^2 = \frac{|E_0|^2}{\omega^2 |\epsilon_1|^2 \eta_0^2} \frac{1}{\rho^2} \sum_{n=-\infty}^{+\infty} \sum_{m=-\infty}^{+\infty} (nm) b_n^{TE} b_m^{TE*} J_n(\beta_1 \rho) J_m(\beta_1 \rho) e^{j(n-m)\phi} \tag{2.52}$$

$$|\vec{E}_{d\phi}^{TE}|^2 = \frac{|E_0|^2|\beta_1|^2}{\omega^2|\epsilon_1|^2\eta_0^2}\sum_{n=-\infty}^{+\infty}\sum_{m=-\infty}^{+\infty} b_n^{TE}b_m^{TE*}J_n'(\beta_1\rho)J_m'(\beta_1\rho)e^{j(n-m)\phi} \tag{2.53}$$

The magnitudes for the $\hat{\rho}$ and $\hat{\phi}$ components can now be substituted into equation (2.49). Using the result from equation (2.43) the following integral is obtain.

$$I_{TE} = \frac{2|E_0|^2|\beta_1|^2}{\omega^2|\epsilon_1|^2\eta_0^2a^2}\left\{\sum_{n=-\infty}^{+\infty}|b_n^{TE}|^2\int_0^a\left[\frac{n^2}{|\beta_1|^2\rho^2}J_n^2(\beta_1\rho) + J_n'^2(\beta_1\rho)\right]\rho d\rho\right\} \tag{2.54}$$

The following Bessel function recursion relations may be used to simplify the above integral:

$$\frac{2n}{\beta_1\rho}J_n(\beta_1\rho) = J_{n-1}(\beta_1\rho) + J_{n+1}(\beta_1\rho) \tag{2.55}$$

$$2J_n'(\beta_1\rho) = J_{n-1}(\beta_1\rho) - J_{n+1}(\beta_1\rho) \tag{2.56}$$

Therefore,

$$\frac{n^2}{|\beta_1^2|\rho^2}J_n^2(\beta_1\rho) = \frac{1}{4}\left[J_{n-1}^2(\beta_1\rho) + 2J_{n-1}(\beta_1\rho)J_{n+1}(\beta_1\rho) + J_{n+1}^2(\beta_1\rho)\right] \tag{2.57}$$

$$J_n'^2(\beta_1\rho) = \frac{1}{4}\left[J_{n-1}^2(\beta_1\rho) - 2J_{n-1}(\beta_1\rho)J_{n+1}(\beta_1\rho) + J_{n+1}^2(\beta_1\rho)\right] \tag{2.58}$$

Substituting equations (2.57) and (2.58) into equation (2.54), the following integral is obtain

$$I_{TE} = \frac{|E_0|^2|\beta_1|^2}{\omega^2|\epsilon_1|^2\eta_0^2a^2}\left\{\sum_{n=-\infty}^{+\infty}|b_n^{TE}|^2\int_0^a\left[J_{n-1}^2(\beta_1\rho) + J_{n+1}^2(\beta_1\rho)\right]\rho d\rho\right\} \tag{2.59}$$

Applying the integral from equation (2.45), we obtain the following closed-form solution for the TE^z polarization assuming a lossless medium.

$$I_{TE} = \frac{|E_0|^2|\beta_1|^2}{2\omega^2|\epsilon_1|^2\eta_0^2}\left\{\sum_{n=-\infty}^{+\infty}|b_n^{TE}|^2\left[J_{n-1}^2(\beta_1a) + J_{n+1}^2(\beta_1a) - J_n(\beta_1a)\left[J_{n-2}(\beta_1a) + J_{n+2}(\beta_1a)\right]\right]\right\} \tag{2.60}$$

2.3.2 Closed-form Solution for Lossy Case

2.3.2.1 Solution for (TM^z) Polarization

Similar for the lossless case, we use equation (2.37) to compute the intensity for the TM^z polarization. The magnitude of the electric field inside the wire must be calculated. Since epsilon is complex for a lossy material, the propagation constant inside the nanowire will also be complex. Using the fact that $J_n^*(\beta_1\rho) = J_n(\beta_1^*\rho)$, the electric field magnitude for the lossy case can be written as:

$$|\vec{E}_d^{TM}|^2 = |E_0|^2 \sum_{n=-\infty}^{+\infty} \sum_{m=-\infty}^{+\infty} b_n^{TM} b_m^{TM*} J_n(\beta_1\rho) J_m(\beta_1^*\rho) e^{j(n-m)\phi} \tag{2.61}$$

Substituting equation (2.61) into equation (2.37) and making use of the result shown in equation (2.43), we obtain:

$$I_{TM} = \frac{2}{a^2}|E_0|^2 \sum_{n=-\infty}^{+\infty} |b_n^{TM}|^2 \int_0^a \rho J_n(\beta_1\rho) J_n(\beta_1^*\rho) d\rho \tag{2.62}$$

Using the following integral from [42]:

$$\int_0^a \rho J_n(\beta_1\rho) J_n(\beta_1^*\rho) d\rho = \frac{(\beta_1 a) J_{n+1}(\beta_1 a) J_n(\beta_1^* a) - (\beta_1^* a) J_n(\beta_1 a) J_{n+1}(\beta_1^* a)}{\beta_1^2 - \beta_1^{2*}} \tag{2.63}$$

Hence, the closed-form solution for the intensity integral in a lossy material for the TM^z polarization is

$$I_{TM} = 2|E_0|^2 \sum_{n=-\infty}^{+\infty} |b_n^{TM}|^2 \frac{(\beta_1 a) J_{n+1}(\beta_1 a) J_n(\beta_1^* a) - (\beta_1^* a) J_n(\beta_1 a) J_{n+1}(\beta_1^* a)}{(\beta_1 a)^2 - (\beta_1^* a)^2} \tag{2.64}$$

2.3.2.2 Solution for (TE^z) Polarization

In order to find a closed-form solution for the intensity integral when the wire is composed of a lossy material, we will need to calculate the integral in equation

(2.49) where the magnitudes of the $\hat{\rho}$ and $\hat{\phi}$ components are given below

$$|\vec{E}_{d\rho}^{TE}|^2 = \frac{|E_0|^2}{\omega^2|\epsilon_1|^2\eta_0^2}\frac{1}{\rho^2}\sum_{n=-\infty}^{+\infty}\sum_{m=-\infty}^{+\infty}(nm)b_n^{TE}b_m^{TE*}J_n(\beta_1\rho)J_m(\beta_1^*\rho)e^{j(n-m)\phi} \tag{2.65}$$

$$|\vec{E}_{d\phi}^{TE}|^2 = \frac{|E_0|^2|\beta_1|^2}{\omega^2|\epsilon_1|^2\eta_0^2}\sum_{n=-\infty}^{+\infty}\sum_{m=-\infty}^{+\infty}b_n^{TE}b_m^{TE*}J_n'(\beta_1\rho)J_m'(\beta_1^*\rho)e^{j(n-m)\phi} \tag{2.66}$$

After substituting the magnitudes for $\hat{\rho}$ and $\hat{\phi}$ components into the intensity integral in equation (2.49) and applying the result in equation from equation (2.43), we obtain

$$I_{TE} = \frac{2|E_0|^2|\beta_1|^2}{\omega^2|\epsilon_1|^2\eta_0^2a^2}\times \left\{\sum_{n=-\infty}^{+\infty}|b_n^{TE}|^2\int_0^a\left[\frac{n^2}{|\beta_1|^2\rho^2}J_n(\beta_1\rho)J_n(\beta_1^*\rho)+J_n'(\beta_1\rho)J_n'(\beta_1^*\rho)\right]\rho d\rho\right\} \tag{2.67}$$

The following Bessel function recursion relations may be used to simplify the above integral:

$$\frac{2n}{\beta_1\rho}J_n(\beta_1\rho) = J_{n-1}(\beta_1\rho)+J_{n+1}(\beta_1\rho) \tag{2.68}$$

$$\frac{2n}{\beta_1^*\rho}J_n(\beta_1^*\rho) = J_{n-1}(\beta_1^*\rho)+J_{n+1}(\beta_1^*\rho) \tag{2.69}$$

$$2J_n'(\beta_1\rho) = J_{n-1}(\beta_1\rho)-J_{n+1}(\beta_1\rho) \tag{2.70}$$

$$2J_n'(\beta_1^*\rho) = J_{n-1}(\beta_1^*\rho)-J_{n+1}(\beta_1^*\rho) \tag{2.71}$$

Multiplying equation (2.68) with (2.69) yields equation (2.72), while multiplying equation (2.70) with (2.71) we obtain equation (2.73)

$$\frac{n^2}{|\beta_1^2|\rho^2}J_n(\beta_1\rho)J_n(\beta_1^*\rho) = \frac{1}{4}\Big[J_{n-1}(\beta_1\rho)J_{n-1}(\beta_1^*\rho)+J_{n-1}(\beta_1\rho)J_{n+1}(\beta_1^*\rho) +J_{n+1}(\beta_1\rho)J_{n-1}(\beta_1^*\rho)+J_{n+1}(\beta_1\rho)J_{n+1}(\beta_1^*\rho)\Big] \tag{2.72}$$

$$J_n'(\beta_1\rho)J_n'(\beta_1^*\rho) = \frac{1}{4}\Big[J_{n-1}(\beta_1\rho)J_{n-1}(\beta_1^*\rho)-J_{n-1}(\beta_1\rho)J_{n+1}(\beta_1^*\rho)$$

$$-J_{n+1}(\beta_1\rho)J_{n-1}(\beta_1^*\rho) + J_{n+1}(\beta_1\rho)J_{n+1}(\beta_1^*\rho)\Big] \tag{2.73}$$

Substituting equations (2.72) and (2.73) into equation (2.67), the following integral is obtained

$$I_{TE} = \frac{|E_0|^2|\beta_1|^2}{\omega^2|\epsilon_1|^2\eta_0^2 a^2}\times \left\{\sum_{n=-\infty}^{+\infty}|b_n^{TE}|^2\int_0^a\Big[J_{n-1}(\beta_1\rho)J_{n-1}(\beta_1^*\rho) + J_{n+1}(\beta_1\rho)J_{n+1}(\beta_1^*\rho)\Big]\rho d\rho\right\} \tag{2.74}$$

Applying the integral from equation (2.63), the expression for the lossy intensity integral for TE^z polarization is:

$$I_{TE} = \frac{|E_0|^2|\beta_1|^2}{\omega^2|\epsilon_1|^2\eta_0^2}\times \left\{\sum_{n=-\infty}^{+\infty}|b_n^{TE}|^2\left[\frac{(\beta_1 a)J_n(\beta_1 a)J_{n-1}(\beta_1^* a) - (\beta_1^* a)J_{n-1}(\beta_1 a)J_n(\beta_1^* a)}{(\beta_1 a)^2 - (\beta_1^* a)^2} + \frac{(\beta_1 a)J_{n+2}(\beta_1 a)J_{n+1}(\beta_1^* a) - (\beta_1^* a)J_{n+1}(\beta_1 a)J_{n+2}(\beta_1^* a)}{(\beta_1 a)^2 - (\beta_1^* a)^2}\right]\right\} \tag{2.75}$$

2.3.3 The Internal Electromagnetic Intensity for a Gallium Phosphide (GaP) Nanowire

The internal electromagnetic intensity for a Gallium Phosphide nanowire will now be calculated. The expressions in the previous section for the internal field intensity were input into a computer program in MATLAB. The computer program was used to calculate the intensity inside a GaP nanowire as a function of the nanowire diameter by calculating the required Bessel functions. In order to calculate the internal electromagnetic intensity numerically, the summation must be truncated to a finite number of terms. For the calculations in this section, we kept the first 30 terms in the summation. Two excitation wavelengths were chosen for this study. The two wavelengths to study were $\lambda = 488$ nm and $\lambda = 514.5$ nm. At these wavelengths the permittivity of GaP is $\epsilon_{r1} = 13.2382 - j0.0003$ and $\epsilon_{r1} = 12.5568$ respectively. We plot the ratio of the TM^z to TE^z intensity as a function of diameter in Figure 2.5. It can be seen for diameters under 125 nm,

the intensity for the TM^z is dominant over the TE^z polarization. This observation agrees well with experimental and Discrete Dipole Approximation (DDA) calculations recently published in [19], where Raman scattering from nanowires was measured and the internal electromagnetic intensity calculated for finite length nanowires. Based on our analytical calculations for infinitely long nanowires, we can see that higher order resonant diameters are predicted. A technique for calculating the angular dependence of the electric field intensity for infinitely long nanowires will be discussed in the next section.

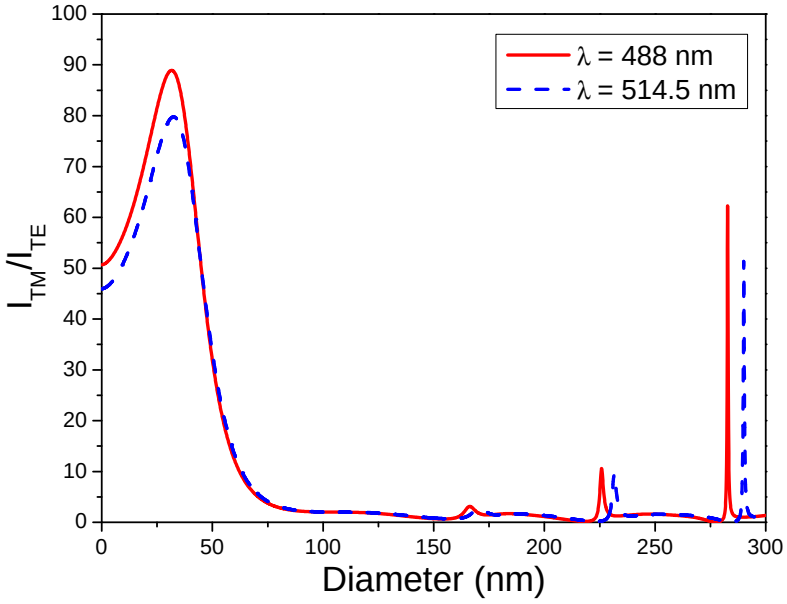

Figure 2.5: I_{TM} / I_{TE} ratio for a GaP nanowire for $\lambda = 418$ nm and $\lambda = 514.5$ nm

2.3.4 Polarization Dependence of Nanowire Intensity

The polarization dependence of a dielectric nanowire at normal incidence exhibits a dependence on both the TM^z and TE^z polarizations. Figure 2.6 shows the geometry for a normally incident wave upon a nanowire at an arbitrary angle θ. In order to consider a normally incident wave at an arbitrary angle, we first recall

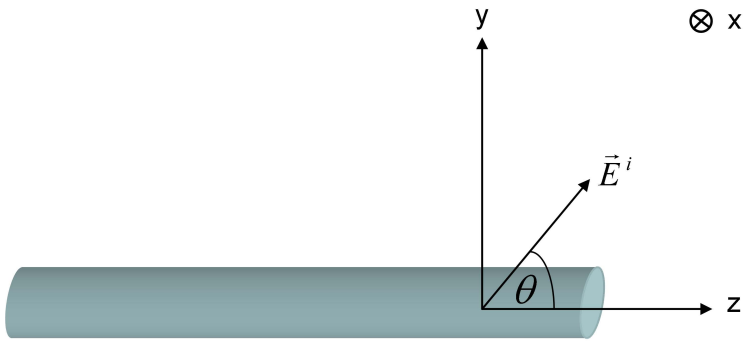

Figure 2.6: Geometry for a normally incident wave upon a nanowire at angle θ

the form of the incident electric field for the TM_z and TE_z polarizations.

$$\vec{E}_i^{TM} = \hat{a_z} E_{iz} e^{-j\beta x} \tag{2.76}$$

$$\vec{E}_i^{TE} = \hat{a_y} E_{iy} e^{-j\beta x} \tag{2.77}$$

As shown in Figure 2.6, an electric field may be incident at an arbitrary angle θ with respect to the wire axis (the $\hat{z}$ axis). Assuming wave propagation along the positive $\hat{x}$ direction, then we may rewrite the incident electric field vector as:

$$\vec{E_i} = \left[|\vec{E_i}| \sin\theta \hat{a}_y + |\vec{E_i}| \cos\theta \hat{a}_z \right] e^{-j\beta x} \tag{2.78}$$

If we assume that $|\vec{E_i}| = E_0 = 1$, then

$$\vec{E_i} = \left[\sin\theta \hat{a}_y + \cos\theta \hat{a}_z \right] e^{-j\beta x} \tag{2.79}$$

This can be considered to be a superposition of the TM^z and TE^z fields, where $E_0 = \cos\,\theta$ for the TM^z case and $E_0 = \sin\,\theta$ for the TE^z case. Next we consider the fields inside the cylinder, which may be expressed in the form

$$\vec{E}_d^{total} = \vec{E}_d^{TM'} + \vec{E}_d^{TE'} = E_{dz}^{TM'} \hat{a}_z + E_{d\rho}^{TE'} \hat{a}_\rho + E_{d\phi}^{TE'} \hat{a}_\phi \tag{2.80}$$

where

$$\vec{E}_d^{TM'} = \vec{E}_d^{TM}|_{E_0 = cos\theta} \tag{2.81}$$

$$\vec{E}_d^{TE'} = \vec{E}_d^{TE}|_{E_0=sin\theta} \tag{2.82}$$

The expressions for $\vec{E}_d^{TM}$ and $\vec{E}_d^{TE}$ are given by equation (2.3) and equation (2.30) respectively. The expression for the intensity due to the contribution of both polarizations may be written from the intensity integral:

$$I_{total} = \frac{1}{\pi a^2} \int_0^a \int_0^{2\pi} |\vec{E}_d^{total}|^2 \rho d\rho d\phi \tag{2.83}$$

We next substitute equation (2.80) into equation (2.83) and obtain

$$I_{total} = \frac{1}{\pi a^2} \int_0^a \int_0^{2\pi} |\vec{E}_{dz}^{TM'}|^2 + |\vec{E}_{d\rho}^{TE'}|^2 + |\vec{E}_{d\phi}^{TE'}|^2 \rho d\rho d\phi \tag{2.84}$$

Examining equation (2.84), we realize this integral can be split into the two intensity integrals (equations (2.37) and (2.49)) evaluated with the appropriate E_0 term from equations (2.81) and (2.82). Thus we obtain

$$I_{total} = I_{TM'} + I_{TE'} = I_{TM} \cos^2\theta + I_{TE} \sin^2\theta \tag{2.85}$$

where I_{TM} and I_{TE} are the expressions for the TM^z and TE^z intensities that we derived previously in sections assuming $E_0 = 1$. Figure 2.7 shows I_{total} calculations for various wire diameters at excitation wavelength $\lambda = 488$ nm. It can be seen for wire diameters below 125 nm, the I_{total} exhibits a $\cos^2\theta$ angular dependence.

2.4 Summary

The classical problem of scattering from an infinitely long dielectric nanowire at normal incidence was solved for the TM^z and TE^z polarizations. The electric field magnitude was calculated for an infinitely long GaP nanowire. The diameter dependence on the internal fields of a dielectric nanowire for lossless and lossy dielectrics was studied based on closed-form analytical solutions to the internal electromagnetic field intensity integral. A computer code was used to calculate the internal electric field intensity for GaP nanowires at optical wavelengths using experimental GaP dielectric properties at these frequencies. The ratio of the I_{TM} to I_{TE} plot versus diameter shows that GaP nanowires have a larger internal

electric field for the TM^z polarization in comparison to the TE^z polarization. This phenomenon was further explored by developing a technique to determine the polarization dependence of the intensity integral at normal incidence. For nanowire diameters where I_{TM} is larger than I_{TE}, GaP nanowires exhibit a $\cos^2\theta$ dependence. These analytical calculations for GaP nanowires at $\lambda = 418$ nm agree well with recently reported experimental data and DDA calculations.

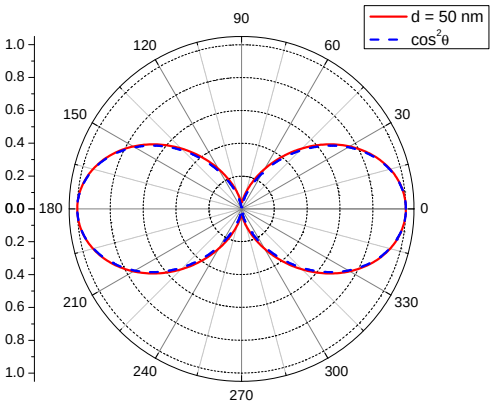

(a) d = 50 nm

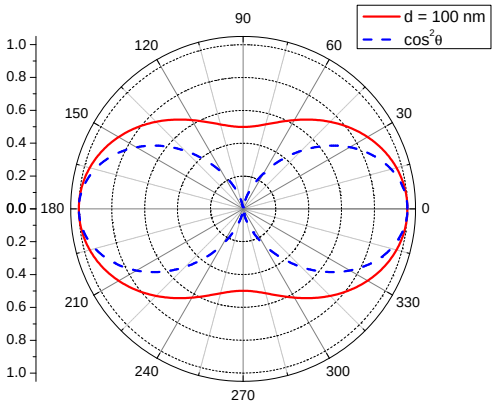

(b) d = 100 nm

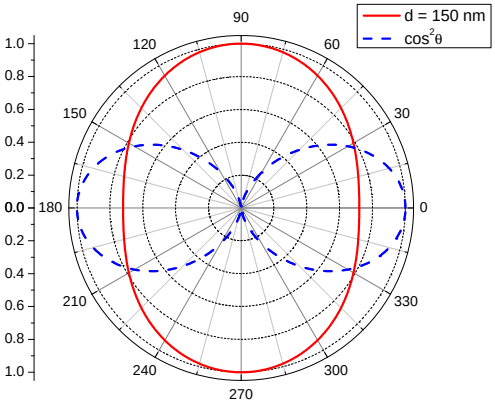

(c) d = 150 nm

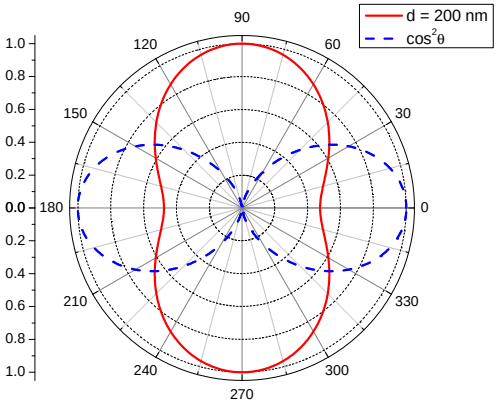

(d) d = 200 nm

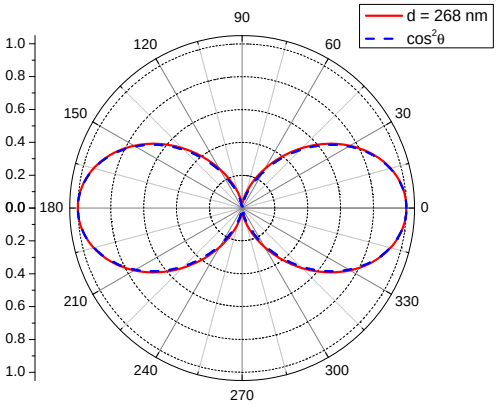

(e) d = 268 nm

Figure 2.7: Normalized polar intensity plots (I_{total}) for a Gallium Phosphide nanowire of various diameters with $\lambda = 488$ nm excitation.

Chapter 3

Surface Impedance Models for Nanoscale Structures

3.1 Introduction

Nanoscale structures such as nanoslabs, nanowires and tubular nanowires have recently become physically realizable due to advances in nano-fabrication technologies. These nanoscale structures are currently being investigated as terahertz devices such as frequency selective surfaces (FSS) and optical antennas. In order to carry out efficient simulation and design of these devices, appropriate electromagnetic models must be developed. These models must include material parameters which account for the dielectric dispersion and losses. In addition, most metals in the infrared and optical frequency regime (e.g. gold and silver) exhibit a negative real part of the dielectric function which must also be included in the model. The use of surface impedance boundary conditions requires that an appropriate surface impedance model be developed, which incorporates both material and geometrical parameters. Surface impedance boundary conditions have recently been applied in the analysis of copper dipoles in the near-infrared [13]. In order to effectively analyze other structures such as nanoslabs and nanotubular wires, appropriate models must be developed and examined for their applicability to various materials and wavelength regimes. Surface impedance models for nanoslabs, nanowires and tubular nanowires will be presented in this chapter. The expressions for sur-

face impedance developed here will incorporate properties of metals in the infrared and optical spectrum based on Lorentz-Drude oscillator models. The asymptotic limits for the surface impedance expressions will be examined in order to show the relationship between each type of structure as well as test the validity of the model. The material models will be incorporated into the surface impedance for each case.

3.2 Surface Impedance Model for a Nanoslab

The most basic surface we can study is a flat surface of a finite thickness. Figure 3.1 depicts the geometry that will be considered for a nanoslab of thickness d. We

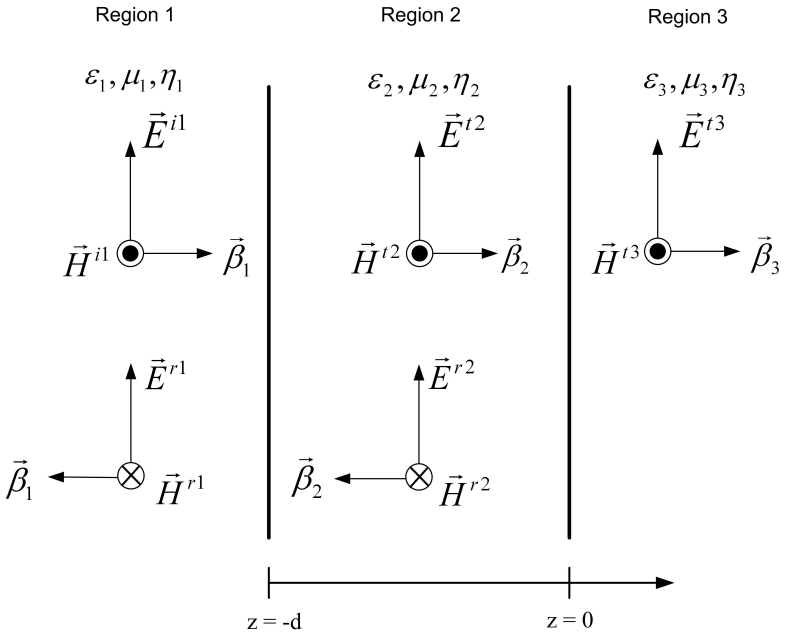

Figure 3.1: Geometry of a nanoslab of thickness d.

may define the surface impedance as

$$Z_{in}(z) = \frac{E^{total}(z)}{H^{total}(z)} \tag{3.1}$$

Calculating the surface impedance at the interface of Region 1 and Region 2 (ie. at $z = -d^+$), the impedance can be expressed mathematically as

$$Z_{in}(z = -d^+) = \eta_2 \left[\frac{1 + \Gamma_{in}(z = 0^-) e^{-2\gamma_2 d}}{1 - \Gamma_{in}(z = 0^-) e^{-2\gamma_2 d}} \right] \tag{3.2}$$

where

$$\gamma_2 = \sqrt{j\omega\mu_2(j\omega\epsilon_2)} = \sqrt{-\omega^2\mu_2\epsilon_2} = j\omega\sqrt{\mu_0\epsilon_0}\sqrt{\epsilon'_{r2} - j\epsilon''_{r2}} \tag{3.3}$$

and

$$\Gamma_{in}(z = 0^-) = \frac{Z_{in}(z = 0^+) - \eta_2}{Z_{in}(z = 0^+) + \eta_2} = \frac{\eta_3 - \eta_2}{\eta_3 + \eta_2} \tag{3.4}$$

Assuming that Region 1 and Region 3 are both free-space, then

$$\eta_1 = \eta_3 = Z_0 = \sqrt{\frac{\mu_0}{\epsilon_0}} \tag{3.5}$$

and the wave impedance of Region 2 is given by

$$\eta_2 = \sqrt{\frac{\mu_2}{\epsilon_2}} = \frac{Z_0}{\sqrt{\epsilon'_{r2} - j\epsilon''_{r2}}} \tag{3.6}$$

After substituting equations (3.5) and (3.6) into (3.4) and substituting equation (3.4) into equation (3.2) and simplifying, the following expression is obtained for the surface impedance of a nanoslab:

$$Z_s = Z_{in}(z = -d) = \frac{Z_0}{\sqrt{\epsilon'_{r2} - j\epsilon''_{r2}}} \left[\frac{\sqrt{\epsilon'_{r2} - j\epsilon''_{r2}} + 1 + \left(\sqrt{\epsilon'_{r2} - j\epsilon''_{r2}} - 1\right) e^{-2\gamma_2 d}}{\sqrt{\epsilon'_{r2} - j\epsilon''_{r2}} + 1 - \left(\sqrt{\epsilon'_{r2} - j\epsilon''_{r2}} - 1\right) e^{-2\gamma_2 d}} \right] \tag{3.7}$$

We note that equation (3.7) accounts for the thickness of the material, while the surface impedance for a half-space (equation (3.8)) in Balanis and Munk does not account for material thickness in Region 2 [38, 43].

$$Z_s = \frac{Z_0}{\sqrt{\epsilon'_{r2} - j\epsilon''_{r2}}} \tag{3.8}$$

In Figure 3.2, we compare numerically the results using the surface impedance models from equations (3.7) and (3.8). A Lorentz-Drude model is used in the numerical computation to determine the complex permittivity of the material. As

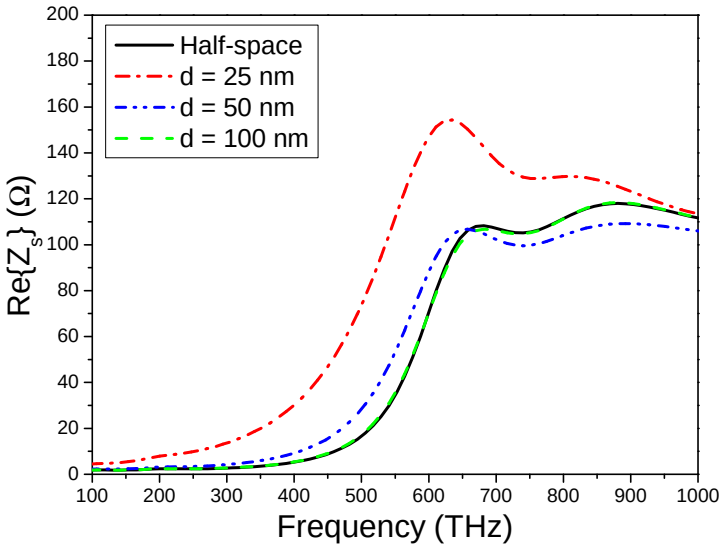

(a) Real component of the surface impedance, Z_s

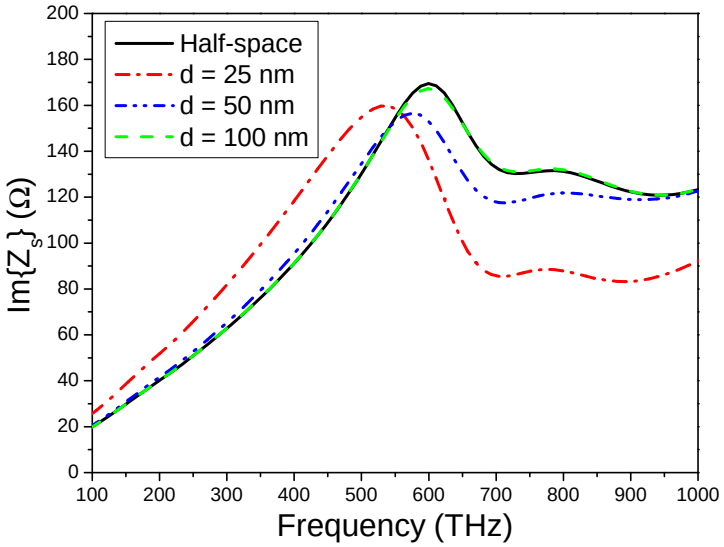

(b) Imaginary component of the surface impedance, Z_s

Figure 3.2: Surface impedance Z_s for a gold nanoslab of varying thickness.

can be seen for a gold nanoslab of thickness d = 25 nm and d = 50 nm, the surface impedance varies significantly between the thin slab surface impedance and the

half-space surface impedance value. Equation (3.7) can be examined asymptotically to determine if the result agrees with the expected value. When the thickness of Region 2 becomes large, it appears as if there is only an interface between Region 1 and Region 2. Hence we expect to obtain the half-space when the thickness (d) of Region 2 becomes large. From equation (3.7), we can see that the $e^{-2\gamma_2 d}$ term will decay rapidly when the thickness d becomes large and reduce to the half-space surface impedance expression equation (3.8). Figure 3.3 shows numerically for a gold slab of thickness $d = 500$ nm, the nanoslab surface impedance model and half-space impedance model agree. For a very thin nanoslab, the exponential term in equation (3.7) may be approximated using a Taylor series expansion and retaining the first term only show below:

$$e^{-2\gamma_2 d} \approx 1 - 2\gamma_2 d \tag{3.9}$$

Substituting this approximation into equation (3.7) and simplifying we obtain the following surface impedance expression for a vanishingly thin nanoslab:

$$Z_s = Z_0 \left[\frac{1 - j\beta_0 d\left(\sqrt{\epsilon'_{r2} - j\epsilon''_{r2}} - 1\right)}{1 - j\beta_0 d\sqrt{\epsilon'_{r2} - j\epsilon''_{r2}}\left(\sqrt{\epsilon'_{r2} - j\epsilon''_{r2}} - 1\right)} \right] \tag{3.10}$$

where $\beta_0 = \omega\sqrt{\mu_0\epsilon_0}$. Examining equation (3.10), it can be seen that for vanishingly thin nanoslab the surface impedance will approach the impedance of free-space Z_0.

3.3 Surface Impedance for a Nanowire

A cylindrical wire is another surface of interest in electromagnetics since it may be used to study nanowires. In order to solve for the surface impedance, there are two approaches that can be considered. The first approach that can be used is to solve for the scattered electric and magnetic fields for an infinite dielectric cylinder. The ratio of the tangential electric and magnetic fields at the surface of the wire will determine the surface impedance. Another method is to solve the homogeneous wave equation for the electric fields inside an infinite wire. The magnetic field can be determined from the electric field using Maxwell's equations. The geometry to be considered for this problem is shown in Figure 3.4. We will use the later

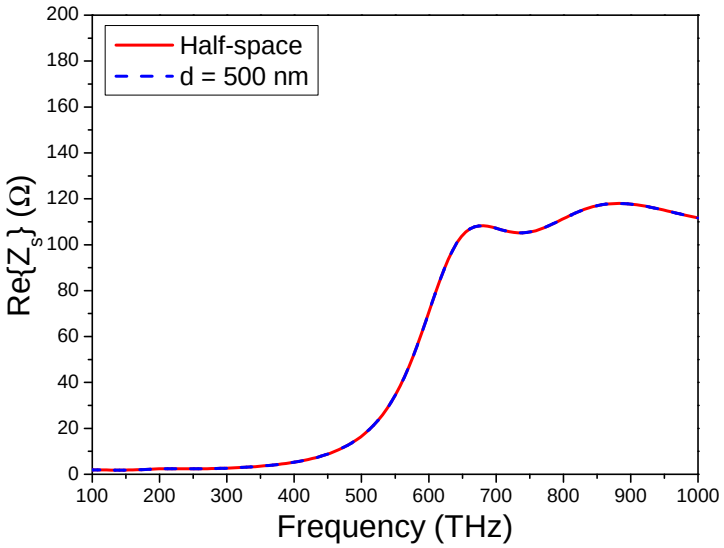

(a) Real component of the surface impedance, Z_s

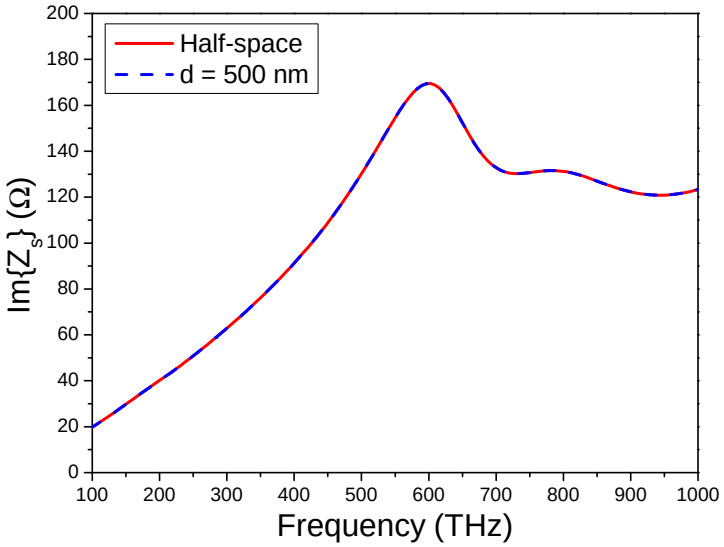

(b) Imaginary component of the surface impedance, Z_s

Figure 3.3: Comparison of surface impedance Z_s values using the half-space expression and the equation (3.7) with thickness $d = 500$ nm.

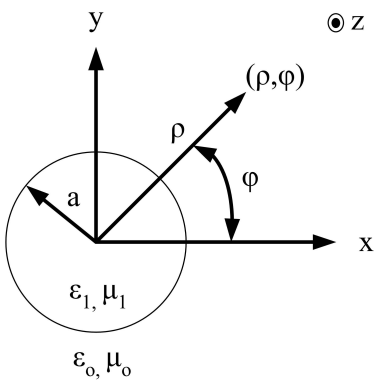

Figure 3.4: Geometry of a nanowire with radius $\rho = a$.

approach to solve for electric field. Assuming the fields exist only along the wire axis and the material outside the wire is free-space, the fields obey the following wave equation [44]:

$$\nabla^2 E_z + \omega^2 \mu \epsilon E_z = 0 \tag{3.11}$$

where

$$\epsilon = \epsilon_0 \epsilon_r = \epsilon_0 \left(\epsilon_r' - j\epsilon_r'' \right) \tag{3.12}$$

In cylindrical coordinates, equation (3.11) becomes

$$\frac{d^2 E_z}{d\rho^2} + \frac{1}{\rho} \frac{dE_z}{d\rho} + \omega^2 \mu \epsilon' E_z = 0 \tag{3.13}$$

A solution to a wave equation of this form exists and has the form

$$E_z(\beta\rho) = AJ_0(\beta\rho) + BY_0(\beta\rho) \tag{3.14}$$

and

$$\beta = \sqrt{\omega^2 \mu \epsilon} = \omega \sqrt{\mu_0 \epsilon_0} \sqrt{\epsilon_r' - j\epsilon_r''} \tag{3.15}$$

where only the zero order modes are retained [44]. In order to solve for the unknown coefficients A and B, we must specify boundary conditions. The coefficients B is set to zero due to a singularity occurring with the Neumann function as the radius ρ approaches zero. The coefficient A can be determined by setting the current

density equal to a constant value at the surface of the wire ($\rho = a$). Hence,

$$A = \frac{E_{z0}}{J_0(\beta a)} \tag{3.16}$$

$$E_z(\beta\rho) = \frac{E_{z0} J_0(\beta\rho)}{J_0(\beta a)} \tag{3.17}$$

With the expression for the electric field known as a function of the radius, the magnetic fields can now be calculated from:

$$H_\phi(\beta\rho) = \frac{1}{j\omega\mu} \frac{dE_z}{d\rho} \tag{3.18}$$

Yielding the following expression for the magnetic field:

$$H_\phi(\beta\rho) = \frac{\beta}{j\omega\mu_0} \frac{E_{z0} J_0'(\beta\rho)}{J_0(\beta a)} \tag{3.19}$$

The surface impedance for a nanowire can be calculated from

$$Z_s = \frac{E_z|_{\rho=a}}{H_\phi|_{\rho=a}} = \frac{j\omega\mu}{\beta} \frac{J_0(\beta a)}{J_0'(\beta a)} = j \frac{Z_0}{\sqrt{\epsilon_r' - j\epsilon_r''}} \frac{J_0(\beta a)}{J_0'(\beta a)} \tag{3.20}$$

where Z_0 is the impedance of free-space given in equation (3.5). Letting $\beta a = jx$, the surface impedance expression in equation (3.20) can be rewritten in terms of the modified Bessel functions using the following relations listed in equations (3.21)-(3.23) [45].

$$J_n(jx) = (j)^n I_n(x) \tag{3.21}$$

$$J_0(jx) = I_0(x) \tag{3.22}$$

$$\frac{d}{d(jx)} J_0(jx) = \frac{dx}{d(jx)} \frac{d}{dx} J_0(jx) = \frac{dx}{d(jx)} \frac{d}{dx} I_0(x) = \frac{dx}{d(jx)} I_0'(x) = -j I_0'(x) \tag{3.23}$$

The surface impedance in terms of modified Bessel functions is then

$$Z_s(x) = \frac{-\omega\mu_0}{\beta} \frac{\beta I_0(x)}{I_0'(x)} \tag{3.24}$$

Equation (3.29) can be simplified one step further using the recursion relation for the modified Bessel function derivative shown below [45]

$$I_n'(x) = \frac{n}{x} I_n(x) + I_{n-1}(x) \tag{3.25}$$

with n = 0, then

$$I_0'(x) = I_{-1}(x) = I_1(x) \tag{3.26}$$

The final expression for the surface impedance in terms of modified Bessel functions is given in equation (3.27) with argument $x = -j\beta a$

$$Z_s(x) = \frac{\omega\mu_0}{\beta} \frac{I_0(x)}{I_1(x)} = \frac{Z_0}{\sqrt{\epsilon_r' - j\epsilon_r''}} \frac{I_0(x)}{I_1(x)} \tag{3.27}$$

Figure 3.5 illustrates how the geometry impacts the surface impedance value. As can be seen there is a large discrepancy between the surface impedance of a half-space and a nanowire. These variations if not accounted for appropriately in the electromagnetic modeling with give large errors between the predicted (simulated) result and the measured result. We next examine the large and small argument approximations to the surface impedance expression in equation (3.27). For the large argument approximation we make use of the following large argument approximation for the modified Bessel function [45]:

$$I_n(x) \approx \frac{e^x}{\sqrt{2\pi x}} \tag{3.28}$$

Substituting the above large argument approximation into equation (3.27), we obtain

$$Z_s(x) \approx \frac{Z_0}{\sqrt{\epsilon_r' - j\epsilon_r''}} \tag{3.29}$$

which is the same as the expression for the surface impedance of a half-space shown in equation (3.8). We use gold material properties and a nanowire of radius $a = 5000$ nm to calculate the results shown in Figure 3.6. Figure 3.6 shows that numerically, equation (3.27) approaches the Balanis expression for the half-space surface impedance as expected for large radii nanowires.

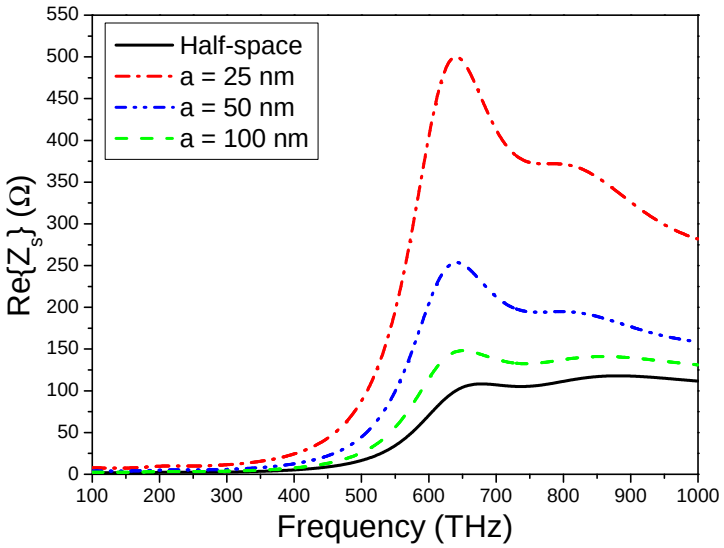

(a) Real component of the surface impedance, Z_s

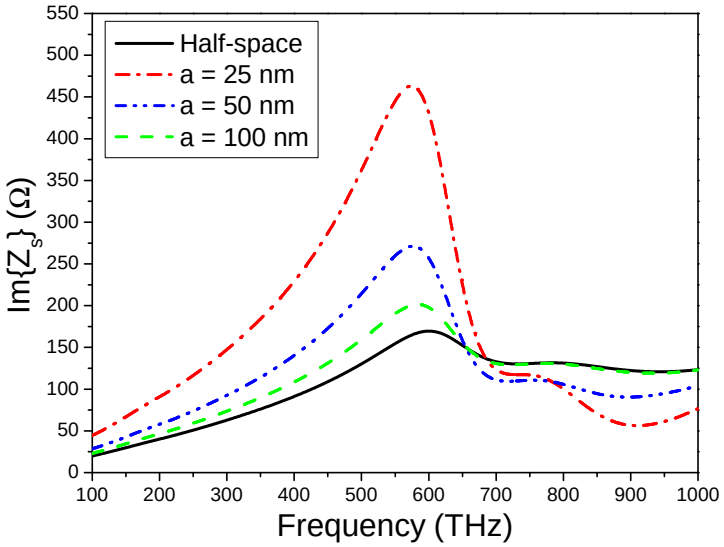

(b) Imaginary component of the surface impedance, Z_s

Figure 3.5: Surface impedance Z_s for a gold nanowire of varying radii.

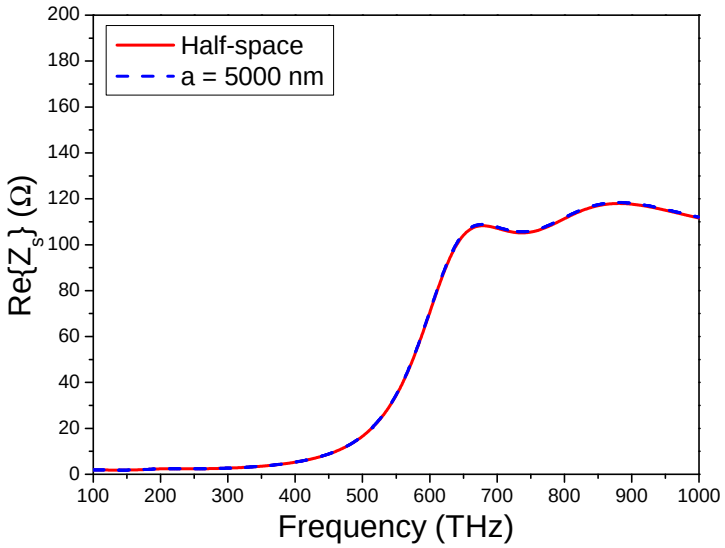

(a) Real component of the surface impedance, Z_s

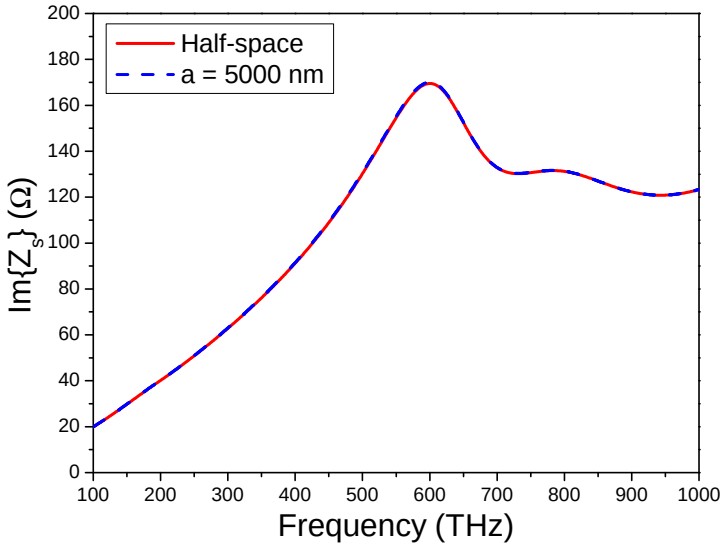

(b) Imaginary component of the surface impedance, Z_s

Figure 3.6: Comparison of surface impedance Z_s values using the half-space expression and the equation (3.27) with radius $a = 5000$ nm.

For a wire of small radius, we may use the small argument approximation for the modified Bessel functions shown below:

$$I_n(x) \approx \frac{\left(\frac{x}{2}\right)^2}{\Gamma(n+1)} \tag{3.30}$$

for $n = 0$ and $n = 1$ we have

$$I_0(x) \approx 1 \tag{3.31}$$

$$I_1(x) \approx \frac{x}{2} \tag{3.32}$$

Substituting equations (3.31) and (3.32) into equation (3.27), we obtain

$$Z_s(x) \approx \frac{2Z_0}{\sqrt{\epsilon_r' - j\epsilon_r''}x} \tag{3.33}$$

where $x = -j\beta a$

3.4 Surface Impedance Model for a Tubular Nanowire

Tubular nanowires are another class of nanoscale structures that are of interest for electromagnetic devices. The surface impedance of a tubular nanowire is of use for examining the properties of coated nanowire structures. The geometry for an infinitely long tubular wire is shown in Figure 3.7. We will also assume that Regions 1 and 3 are free-space (ie. $\epsilon_1 = \epsilon_3 = \epsilon_0$ and $\mu_1 = \mu_3 = \mu_0$). The electric fields inside the tubular wire satisfy the wave equation:

$$\nabla^2 E_{zn} + \omega^2 \mu_n \epsilon_n E_{zn} = 0 \tag{3.34}$$

where we assume the electric fields inside the tubular nanowire are $\hat{z}$-directed only and the permittivity in region n is given by

$$\epsilon_n = \epsilon_0 \epsilon_r = \epsilon_0 \left(\epsilon_{rn}' - j\epsilon_{rn}''\right) \tag{3.35}$$

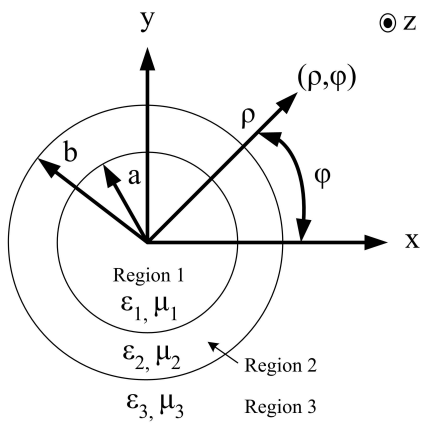

Figure 3.7: Geometry for a tubular nanowire with inner radius $\rho = a$ and outer radius $\rho = b$.

Solutions to the above wave equation inside Region 1 have the form shown below in equation (3.36) where only the zero order modes are retained:

$$E_{z1}(\beta_1\rho) = A_1 J_0(\beta_1\rho) \tag{3.36}$$

In Region 2, the solution for the electric field is a superposition of inward and outward traveling Hankel functions.

$$E_{z2}(\beta_2\rho) = A_2 H_0^{(1)}(\beta_2\rho) + B_2 H_0^{(2)}(\beta_2\rho) \tag{3.37}$$

where

$$\beta_1 = \omega\sqrt{\mu_0\epsilon_0} \tag{3.38}$$

and

$$\beta_2 = \omega\sqrt{\mu_0\epsilon_0}\sqrt{\epsilon'_{r2} - j\epsilon''_{r2}} \tag{3.39}$$

The tangential magnetic fields in Region n can be calculated from

$$H_{\phi n}(\beta_n\rho) = \frac{1}{j\omega\mu_0}\frac{dE_{zn}}{d\rho} \tag{3.40}$$

Hence, the magnetic fields in Regions 1 and 2 are given by:

$$H_{\phi 1}(\beta_1\rho) = \frac{1}{j\omega\mu_0}\frac{dE_{z1}}{d\rho} = \frac{\beta_1 A_1}{j\omega\mu_0}J'_0(\beta_1\rho) \tag{3.41}$$

and

$$H_{\phi 2}(\beta_2\rho) = \frac{1}{j\omega\mu_0}\frac{dE_{z2}}{d\rho} = \frac{\beta_2}{j\omega\mu_0}\left[A_2 H_0^{(1)'}(\beta_2\rho) + B_2 H_0^{(2)'}(\beta_2\rho)\right] \tag{3.42}$$

We next apply boundary conditions at the boundary between Region 1 and Region 2 (ie. $\rho = a$) to solve for the unknown coefficients. The tangential electric and magnetic fields must be continuous at the boundary, hence

$$E_{z1}|_{\rho=a} = E_{z2}|_{\rho=a} \tag{3.43}$$

$$H_{\phi 1}|_{\rho=a} = H_{\phi 2}|_{\rho=a} \tag{3.44}$$

Substituting in equations (3.36)-(3.37) into (3.43) and (3.41)-(3.42) into (3.44), we obtain the following two equations:

$$A_1 J_0(\beta_1 a) = A_2 H_0^{(0)}(\beta_2 a) + B_2 H_0^{(2)}(\beta_2 a) \tag{3.45}$$

$$\beta_1 A_1 J_0'(\beta_1 a) = \beta_2\left[A_2 H_0^{(1)'}(\beta_2 a) + B_2 H_0^{(2)'}(\beta_2 a)\right] \tag{3.46}$$

The surface impedance is given for a tubular wire is given by the ratio of the tangential electric and magnetic fields at the outer boundary ($\rho = b$). In equation form, this may be expressed as

$$Z_s = \frac{E_{z2}|_{\rho=b}}{H_{\phi 2}|_{\rho=b}} \tag{3.47}$$

The coefficient A_1 can be expressed in terms of the coefficients A_2 and B_2 by using equation (3.46). Substituting the expression for A_1 in terms of A_2 and B_2 into equation (3.45), B_2 may be determined in terms of A_2. This relation is shown below:

$$B_2 = \left[\frac{\beta_2 H_0^{(1)'}(\beta_2 a) J_0(\beta_1 a) - \beta_1 H_0^{(0)}(\beta_2 a) J_0'(\beta_1 a)}{\beta_1 H_0^{(2)}(\beta_2 a) J_0'(\beta_1 a) - \beta_2 J_0(\beta_1 a) H_0^{(1)'}(\beta_2 a)}\right] A_2 \tag{3.48}$$

Equation (3.48) may be substituted into the expressions for the electric and magnetic fields in Region 2. The surface impedance is determined by using (3.47) where the unknown coefficients cancel in the quotient and yield the following expression

for the surface impedance:

$$Z_s = \frac{j\omega\mu_0}{\beta_2} \frac{H_0^{(1)}(\beta_2 b)X_1 + H_0^{(2)}(\beta_2 b)X_2}{H_0^{(1)'}(\beta_2 b)X_1 + H_0^{(2)'}(\beta_2 b)X_2} \tag{3.49}$$

After applying the Hankel function recursion relations for the derivative, the coefficients X_1 and X_2 may be written as

$$X_1 = \beta_2 J_0(\beta_1 a)H_1^{(2)}(\beta_2 a) - \beta_1 J_1(\beta_1 a)H_0^{(2)}(\beta_2 a) \tag{3.50}$$

$$X_2 = \beta_1 J_1(\beta_1 a)H_0^{(1)}(\beta_2 a) - \beta_2 J_0(\beta_1 a)H_1^{(1)}(\beta_2 a) \tag{3.51}$$

and the surface impedance for a tubular nanowire is given by:

$$Z_s = -\frac{j\omega\mu_0}{\beta_2} \frac{H_0^{(1)}(\beta_2 b)X_1 + H_0^{(2)}(\beta_2 b)X_2}{H_1^{(1)}(\beta_2 b)X_1 + H_1^{(2)}(\beta_2 b)X_2} \tag{3.52}$$

The surface impedance for a tubular wire was first developed by King. King's expression differs from the above expression and is shown below [46]:

$$Z_s = \frac{j\omega\mu_0}{\beta_2} \frac{J_0(\beta_2 a)Y_1(\beta_2 b) - Y_0(\beta_2 a)J_1(\beta_2 b)}{J_1(\beta_2 a)Y_1(\beta_2 b) - Y_1(\beta_2 a)J_1(\beta_2 b)} \tag{3.53}$$

Using the Lorentz-Drude model for gold to generate the complex permittivity, the surface impedance expression for a tubular nanowire and the King expression for the surface impedance may be computed. Figure 3.8 shows a numerical comparison of the tubular nanowire surface impedance formulation with King's formulation. It can be seen that the two formulations give different results for a thin shell tubular nanowires. This difference is due to the a different boundary condition being applied at the inner radius ($\rho = a$). In King's formulation the electric field vanishes at the inner radius, however in the formulation in this work no conditions are placed on the electric field value at the inner radius.

We now consider the case of a tubular nanowire as the inner radius a becomes small. For small radius a, we must apply the small argument approximations for

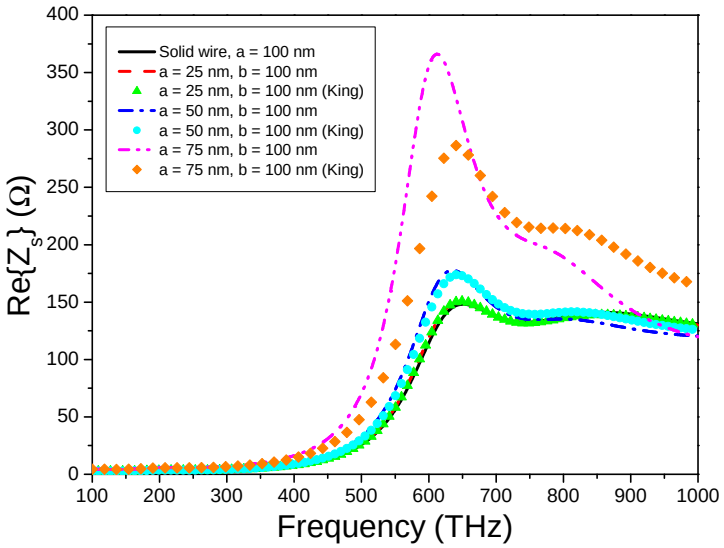

(a) Real component of the surface impedance, Z_s

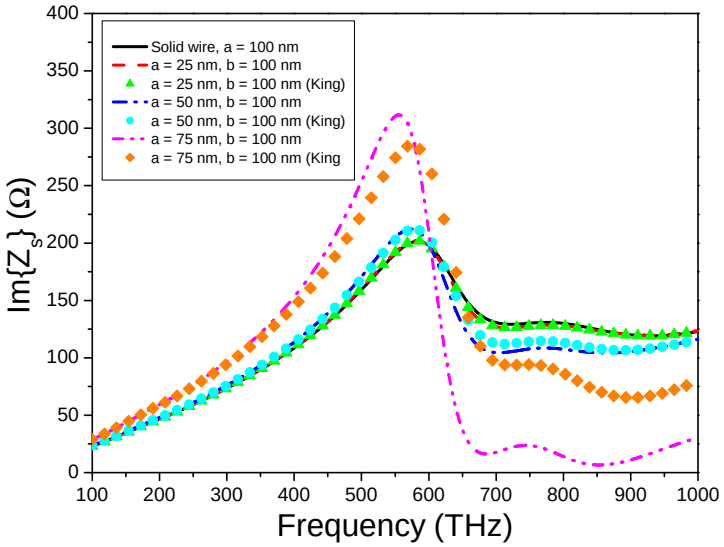

(b) Imaginary component of the surface impedance, Z_s

Figure 3.8: Surface impedance Z_s for a gold tubular nanowire of varying inner radii and constant outer radius.

Bessel and Hankel functions in equations (3.50) and (3.51) shown below [38]:

$$J_0(x) \approx 1 \tag{3.54}$$

$$Y_0(x) \approx \frac{2}{\pi}\ln\big(\frac{\gamma x}{2}\big) \tag{3.55}$$

$$J_1(x) \approx \frac{x}{2} \tag{3.56}$$

$$Y_1(x) \approx -\frac{2}{\pi x} \tag{3.57}$$

Therefore,

$$H_0^{(1)}(x) \approx 1 + j\frac{2}{\pi}\ln\big(\frac{\gamma x}{2}\big) \tag{3.58}$$

$$H_0^{(2)}(x) \approx 1 - j\frac{2}{\pi}\ln\big(\frac{\gamma x}{2}\big) \tag{3.59}$$

$$H_1^{(1)}(x) \approx \frac{x}{2} - j\frac{2}{\pi x} \tag{3.60}$$

$$H_1^{(2)}(x) \approx \frac{x}{2} + j\frac{2}{\pi x} \tag{3.61}$$

Substituting equations (3.54), (3.56) and (3.58)-(3.61) into (3.50)-(3.51) and taking the limit as a goes to zero, equation (3.52) becomes

$$Z_s = \frac{j\omega\mu_0}{\beta_2}\frac{J_0(\beta_2 b)}{J_0'(\beta_2 b)} = j\frac{Z_0}{\sqrt{\epsilon_{r2}' - j\epsilon_{r2}''}}\frac{J_0(\beta_2 b)}{J_0'(\beta_2 b)} \tag{3.62}$$

which is the same expression as the surface impedance for a nanowire (equation (3.20)). It can also be shown that by taking the limit of the above expression for the surface impedance as b becomes large, we will obtain the surface impedance expression for a half-space.

3.5 Summary

We have developed surface impedance expressions for three types of nanostructures in this chapter: nanoslabs, nanowires and tubular nanowires. The surface impedance was calculated by taking the ratio of the electric field and magnetic field at the boundary of the structure. The dispersive nature of materials at the

infrared and optical spectrum are incorporated into the surface impedance models through the permittivity. Asymptotic analysis of these surface impedance expressions provide expected results for the three nanostructures considered. These surface impedance models can be used to efficiently analyze nanoscale structures efficiently. The application of surface impedance models for studying nanowire dipoles will be discussed in the Chapter 4 and the required modification to the integral equation will be explained.

Chapter 4

Modeling of Nanoscale Dipole Antennas

4.1 Introduction

The dipole is the most basic antenna element. In order to study properties of dipole antennas, it is necessary to determine the current distribution on the dipole. The current distribution on a dipole can be determined by solving an integral equation. In this chapter, the moment method for solving the integral equation for the current distribution on a dipole will be explained. Modifications to the moment method formulation will be discussed in order to accommodate the non-idealities of nanoscale dipole antennas at infrared and optical frequencies. The method of moments will be applied to gold and silver nanowire dipole antennas and a nanoscale perfectly electrically conducting (PEC) dipole. Comparisons will be made between the moment method code and commercially available codes for gold and silver nano-dipole antennas.

4.2 Method of Moment Formulation

The method of moments technique was first applied to antenna analysis by Harrington in the late 1960s [47, 48]. The moment method is useful technique for solving electromagnetics problems because it reduces an integral equation into a

system of linear equations. For dipole antennas, we wish to solve the integral equation for the current distribution along the wire. Once the current distribution is known, useful antenna parameters such as the impedance and radiation pattern may be determined. For a perfectly conducting dipole antenna, we wish to solve the following integral equation for the current on surface of the wire [49]:

$$\int I(z')K(z,z')dz' = E^t(z) - E^i(z) \tag{4.1}$$

where $I(z')$ represents the current along the wire, $K(z,z')$ is the kernel, $E^t(z)$ is the tangential field, and $E^i(z)$ is the incident electric field. However for a perfectly conducting dipole antenna, the tangential electric field must be zero on the surface of the dipole, hence equation (4.1) becomes

$$\int I(z')K(z,z')dz' = -E^i(z) \tag{4.2}$$

In order to accurately model nanowire antennas in the infrared and optical range, the material's dispersive properties must be included into the modeling approach. The method of moments technique allows for the lossy nature of materials to be accounted for by using a surface impedance model. In Chapter 3, we developed a surface impedance model for nanowires in the infrared and optical spectrum. To account for losses, integral equation in equation (4.1) must be modified since the tangential fields containing a surface impedance loss model is shown in equation (4.3).

$$\int I(z')K(z,z')dz' = -E^i(z) + Z_s I(z) \tag{4.3}$$

where Z_s is the surface impedance. The current in the above integral equation is expressed in terms of a set of known weighting functions with unknown coefficients. The selection of the weighting functions is important in order to generate a computational efficient code. Since it is anticipated that the current on a nanowire will be similar to that of a perfectly conducting dipole, sinusoidal weighting functions will be used in the moment method approach. A linear set of algebraic equations is formed by evaluating the inner product of the weighting functions with testing functions and enforcing the integral equation at each segment location. The testing functions can differ from the basis functions, but in our implementation a Galerkin

method was selected where both the weighting and testing function are sinusoidal. The moment method using a surface impedance model will result in the equations [49]:

$$\sum_{n=1}^{N} Z'_{mn} I_n = V_m \tag{4.4}$$

where

$$Z'_{mn} = Z_{mn} - \frac{Z_s}{2\pi a} \int_{(m,n)} I_n(z) I_m(z) dz \tag{4.5}$$

In equation (4.5), $I_n(z)$ and $I_m(z)$ represent the weighting and testing functions respectively. The region (m, n) indicates the portion of the wire surface shared by testing function m and weighting function n. The term Z_{mn} is inner product of the testing and weighting function integrated over a segment. The number of segments along the wire is determine by the parameter N. The excitation of the antenna V_m is

$$V_m = E_z^i(z_m) \tag{4.6}$$

We may write equation (4.4) in matrix form as

$$\big[Z_{mn}\big]\big[I_n\big] = \big[V_m\big] \tag{4.7}$$

Hence, the current can be determined using matrix inversion

$$\big[I_n\big] = \big[Z_{mn}\big]^{-1}\big[V_m\big] \tag{4.8}$$

Based on the above equations, a moment code has been developed for studying nanowires. Recall the surface impedance expression for nanowires derived in Chapter 3 shown in equation (4.9). The surface impedance for nanowires will utilize a Lorentz-Drude model to describe the material parameters of the non-ideal nanodipole.

$$Z_s = -\frac{jZ_0}{\sqrt{\epsilon'_r - j\epsilon''_r}} \frac{J_0(\omega\sqrt{\mu_0\epsilon_0}\sqrt{\epsilon'_r - j\epsilon''_r}a)}{J_1(\omega\sqrt{\mu_0\epsilon_0}\sqrt{\epsilon'_r - j\epsilon''_r}a)} \tag{4.9}$$

4.3 Simulation of Nano-Dipole Antennas

In this section we will calculate the input impedance for a nanowire dipole made of Gold and Silver. The geometry of the dipole is shown in Figure 4.1 where the diameter of the wire is $2a$, the length is L and the feed gap size is g. Since the

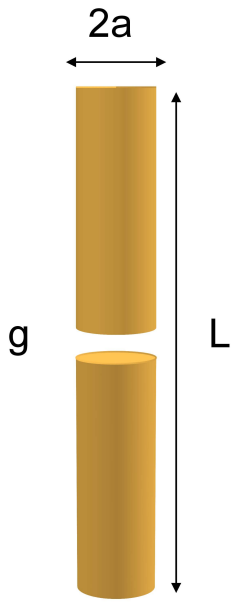

Figure 4.1: Nanowire dipole dimensions.

thin-wire kernel is used in the method of moments implementation, the wire radius must be kept to be less than 0.01 λ ($a < 0.01\lambda$). We will examine a dipole at infrared frequencies ranging from 25 THz - 300 THz which correspond to wavelengths from 1.2 μm to 6 μm. The dipole has length $L = 1.5\mu$m and radius $a = 10$ nm. In the method of moments formulation discussed in the previous section the number of segments along the wire is chosen by the parameter N. It was determined that results in the method of moments converge when setting the number of segments to 100. The gap size in the dipole was chosen to be equal to one segment length or 15 nm. The method of moment formulation was compared to FEKO, a commercial based method of moment code [50]. The results of this comparison are shown in Figure 4.2 which shows very good agreement between the method of moments calculations and FEKO. The resonant frequency and real part of the input impedance at these frequencies for PEC, Gold and Silver nano-dipoles is

shown in Tables 4.1-4.3.

Table 4.1: Resonant frequencies and input impedance for a PEC nano-dipole using FEKO and MoM.

FEKO		*MoM*	
Frequency (THz)	Re{Z_{in}} (Ω)	Frequency (THz)	Re{Z_{in}} (Ω)
93.1	70.9	93.1	72.2
157	857	163	877
292	109	291	106

Table 4.2: Resonant frequencies and input impedance for a Gold nano-dipole using FEKO and MoM.

FEKO		*MoM*	
Frequency (THz)	Re{Z_{in}} (Ω)	Frequency (THz)	Re{Z_{in}} (Ω)
46.4	193	44.9	185
75.6	2645	76.3	2687
129	229	126	221
153	1718	154	1846
199	285	194	272
218	1000	219	1122
261	303	253	278
274	807	273	931

Table 4.3: Resonant frequencies and input impedance for a Silver nano-dipole using FEKO and MoM.

FEKO		*MoM*	
Frequency (THz)	Re{Z_{in}} (Ω)	Frequency (THz)	Re{Z_{in}} (Ω)
46.4	148	46.6	154
78.5	2942	80.3	3103
132	150	130	148
159	2257	160	2420
207	184	201	172
229	1423	229	1539
271	215	263	208
288	942	288	1104

The non-idealities of gold and silver in the infrared impact the resonance frequency of the dipole and the real and imaginary components of the input impedance. Unlike a dipole in the RF, the PEC model of a nanoscale dipole will not provide a good approximation of a nanowire dipole composed of real materials. This is due to the fact that metals at infrared and optical frequencies no longer exhibit "good conductor" properties and act more like lossy dielectrics. Applying the surface impedance model to nanowire dipoles is important in order to account for this effects.

4.4 Summary

An overview of the moment method technique for solving electromagnetic problems was presented. For nanowire dipoles, a nanowire surface impedance containing the material properties of the nanowire must be used. The nanowire surface impedance model was applied to studying gold and silver nanowire dipoles using a Galerkin method of moments code and FEKO. The method of moments and FEKO results show good agreement for PEC, gold and silver nanoscale dipoles. It was determined that gold and silver nanowire dipoles exhibit behavior very different from the PEC nanodipole behavior which differs from our knowledge of dipole antennas in the RF and microwave spectrum.

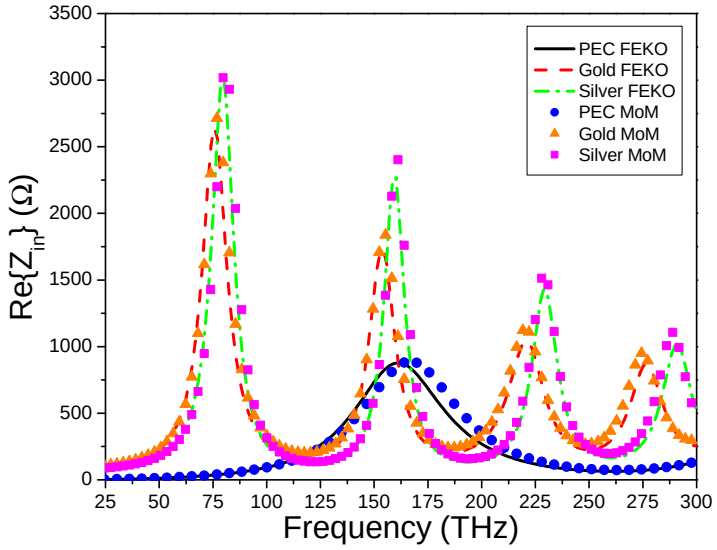

(a) Real component of the input impedance for the nanoscale dipole, Z_{in}

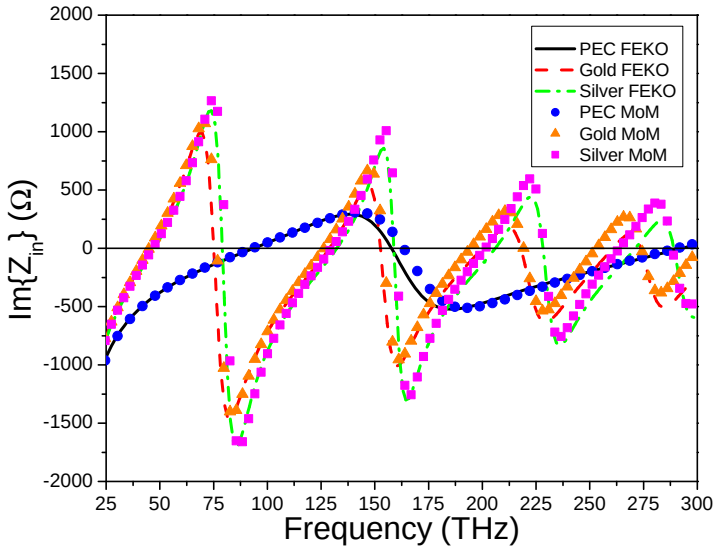

(b) Imaginary component of the input impedance for the nanoscale dipole, Z_{in}

Figure 4.2: Input impedance for a PEC, Gold and Silver nanowire dipole calculated using FEKO and Method of Moments.

Chapter 5

Conclusions

5.1 Summary and Conclusions

In this thesis, nanowires made of semiconducting and metallic materials were studied. The dielectric properties of semiconducting and metals in the infrared and optical spectrum were studied using experimental data and oscillator models such as the Lorentz-Drude model. The particle swarm optimization algorithm was introduced and applied to parameter fitting of a Lorentzian oscillator model which may be used to input dispersive material properties into a finite-difference time-domain electromagnetic modeling code. The PSO technique was used to parameter fit a Lorentzian model for Gallium Phosphide, but may be used to fit parameters for other materials given experimental data. Scattering from infinitely long dielectric wire was applied to a Gallium Phosphide nanowire using the well-known analytical solution.

The electric field magnitude was calculate for GaP nanowires of varying radii for transverse magnetic and transverse electric polarizations. Closed-form solutions for the electromagnetic intensity inside lossless and lossy nanowires were derived and applied to GaP nanowires. The ratio of the intensity for TM^z to TE^z was examined as a function of diameter and it was determined that for diameters under 125 nm, the electric fields in TM^z gave a resonant response. Additional resonances occur within the nanowire for larger diameter wire depending on the product of the wavenumber and wire diameter. The polarization dependence at normal inci-

dence of the electric fields inside the wire was calculated from the contributions of transverse magnetic and transverse electric polarizations and the incidence angle. For diameters where the I_{TM} to I_{TE} ratio is large, a dipole-like pattern ($\cos^2\theta$) was observed when the intensity is plotted as a function of angle. This polarization dependence agrees very well with experimental analysis performed by Professor Peter Eklund's group.

Surface impedance models were examined for simulating nanostructures. Surface impedance models are of interest because they provide a computationally efficient means of simulating a nanoscale structure without the need for fine meshing. In this thesis, surface impedance models for nanoslabs, nanowires and tubular nanowires were derived. In the case of the nanoslab, we examined a dielectric material with variable thickness surrounded by free-space on both sides. This surface impedance model incorporates slab thickness which can be used in the design and optimization of thin metallic patches for infrared and optical frequency selective surfaces. Nanowire and tubular nanowire surface impedance models were derived and examined asymptotically. The nanowire surface impedance model was incorporated into a method of moments code and FEKO. Due to the properties of metals in the infrared and optical, the input impedance for a nanowire dipole varies dramatically from that of a perfectly conducting dipole.

5.2 Future Work

We have examined the properties of nanowires in the infrared and optical spectrum using analytical solutions for scattering from cylinders and surface impedance models. Nanowire modeling using other methods such as finite-element and finite-difference time-domain also should be studied to validate the surface impedance models. Electromagnetic modelings tools which are able to finely grid metallic structures at infrared and optical wavelengths are still underdevelopment. These models can then be used to develop novel infrared and optical devices.

One hypothetical device to be studied infrared or optical detector coupled to a high-frequency diode for solar energy harvesting and light detection. A nanoscale

dipole may be attached to a high-frequency diode. The length of the dipole controls the operating frequency of the detector. Using the surface impedance model, the input impedance can be predicted such that a matching structure to the high-frequency diode can be designed for maximum power transfer. More complex antenna elements with wider bandwidth such as an open-sleeve dipole may be considered for use as infrared and optical detectors. Nanowire modeling techniques can also be used to design optical bio-detection devices. The large fields that occur due to light excitation on nanoscale metallic structures is well known. Exploiting these large fields, molecules may be excited and fluoresce. Due to their small size, nanoscale structures are optimal devices for selectively exciting small molecules for bio-sensing application. Further development in nanoscale electromagnetic modeling methods will enable the design and optimization of nanoscale structures for infrared and bio-detectors to occur prior to fabrication.

In this work, only a few metals (Ag and Au) and semiconductors (GaP) were considered. Several other metals and semiconductors may be studied for their use in nanoscale electromagnetic devices. In addition, the doping of semiconductors can provide additional flexibility when designing novel infrared and optical electromagnetic devices. Using the particle swarm optimization algorithm discussed in this work, parameters for material models may be determined for incorporation into FDTD modeling codes. Investigating other metallic and semiconducting materials through electromagnetic modeling can lead to a better understanding of which materials provide good performance for infrared and optical electromagnetic devices. Using this library of materials, optimization methods such as the genetic algorithm or particle swarm optimization algorithm may be used to optimize the material selection and device dimensions for enhancing device performance.

Bibliography

[1] R. P. Drupp, J. A. Bossard, Y. Ye, D. H. Werner, and T. S. Mayer, "Dual-band infrared single-layer metallodielectric photonic crystals," *Appl. Phys. Lett.*, vol. 85, no. 10, pp. 1835–1837, September 2004.

[2] Y. Tang, J. A. Bossard, D. H. Werner, and T. S. Mayer, "Single-layer metallodielectric nanostructures as dual-band midinfrared filters," *Appl. Phys. Lett.*, vol. 92, no. 26, pp. 263 106–1 – 263 106–3, July 2008.

[3] Z. F. Ren, Z. P. Huang, J. W. Xu, J. H. Wang, P. Bush, M. P. Siegal, and P. N. Provencio, "Synthesis of large arrays of well-aligned carbon nanotubes on glass," *Science*, vol. 282, no. 5391, pp. 1105–1107, November 1998.

[4] T. R. Kline, M. Tian, J. Wang, A. Sen, M. W. H. Chan, and T. E. Mallouk, "Receiving and transmitting light-like radio waves: Antenna effect in arrays of aligned carbon nanotubes," *Inorg. Chem.*, vol. 45, pp. 7555–7565, 2006.

[5] R. Gupta, Q. Xiong, G. D. Mahan, and P. C. Eklund, "Surface optical phonons in gallium phosphide nanowires," *Nano. Lett.*, vol. 12, no. 3, pp. 1745–1750, 2003.

[6] Y. Wang, K. Kempa, B. Kimball, J. B. Carlson, G. Benham, W. Z. Li, T. Kempa, J. Rybczynski, A. Herczynski, and Z. F. Ren, "Receiving and transmitting light-like radio waves: Antenna effect in arrays of aligned carbon nanotubes," *Appl. Phys. Lett.*, vol. 85, September 2004.

[7] G. W. Hanson, "Fundametal transmitting properties of carbon nanotube antennas," *IEEE Trans. Antennas Propag.*, vol. 53, no. 11, pp. 3426–3435, November 2005.

[8] ——, "Current on an infintely-long carbon nanotube antennas excited by a gap generator," *IEEE Trans. Antennas Propag.*, vol. 54, no. 1, pp. 76–81, January 2006.

[9] J. Hao and G. W. Hanson, "Infrared and optical properties of carbon nanotube dipole antennas," *IEEE Trans. Nanotechnol.*, vol. 5, no. 6, pp. 76–81, November 2006.

[10] G. W. Hanson and P. Smith, "Modeling the optical interactions between a carbon nanotube and a plasmon resonant sphere," *IEEE Trans. Antennas Propag.*, vol. 55, no. 11, pp. 3063–3069, November 2007.

[11] P. J. Burke, S. Li, and Z. Yu, "Quantitative theory of nanowire and nanotube antenna performance," *IEEE Trans. Nanotechnol.*, vol. 5, no. 4, pp. 314–334, July 2006.

[12] S. K. Gray and T. Kupka, "Propagation of light in metallic nanowire arrays: Finite-difference time-domain studies of silver cylinders," *Phys. Rev. B*, vol. 68, pp. 045 415–1 – 045 415–11, 2003.

[13] G. W. Hanson, "On the applicability of the surface impedance integral equation for optical and near infrared copper dipole antennas," *IEEE Trans. Antennas Propag.*, vol. 54, no. 12, pp. 3677–3685, December 2006.

[14] V. A. Podolskiy, A. K. Sarychev, E. E. Narimanov, and V. M. Shalaev, "Resonant light interaction with plasmonic nanowire systems," *J. Opt. A: Pure Appl. Opt.*, vol. 7, pp. S32–S37, 2005.

[15] H. Ditlbacher, H. Hohenau, D. Wagner, U. Kreibig, M. Rogers, F. Hofer, F. R. Aussenegg, and J. R. Krenn, "Silver nanowires as surface plasmon resonators," *Phys. Rev. Lett.*, vol. 95, pp. 257 403–1 – 257 403–4, 2005.

[16] L. Cao, B. Nabet, and J. E. Spanier, "Enhanced raman scattering from individual semiconductor nanocones and nanowires," *Phys. Rev. Lett.*, vol. 96, pp. 157 402–1 – 157 402–4, 2006.

[17] L. Cao, L. Laim, P. D. Valenzuela, B. Nabet, and J. E. Spanier, "On the raman scattering from semiconducting nanowires," *J. Raman Spectrosc.*, vol. 38, pp. 697–703, 2007.

[18] Q. Xiong, G. Chen, H. R. Gutierrez, and P. C. Eklund, "Raman scattering studies of individual polar semiconducting nanowires: phonon splitting and antenna effects," *Appl. Phys. A*, vol. 8, no. 5, pp. 299–305, 2008.

[19] G. Chen, J. Wu, Q. Lu, H. R. Gutierrez, Q. Xiong, M. E. Pellen, J. S. Petko, D. H. Werner, and P. C. Eklund, "Optical antenna effect in semiconducting nanowires," *Nano. Lett.*, vol. 8, no. 5, pp. 1341–1346, 2008.

[20] M. S. Hu, H.-L. Chen, C.-H. Shen, L.-S. Hong, B.-R. Huang, K.-H. Chen, and L.-C. Chen, "Photosensitive gold-nanoparticle-embedded dielectric nanowires," *Nature Mater.*, vol. 5, pp. 102–106, February 2006.

[21] K. B. Crozier, A. Sundaramurthy, G. S. Kino, and C. F. Quate, "Optical antennas: Resonators for local field enhancement," *J. Appl. Phys.*, vol. 94, no. 7, pp. 884–889, October 2003.

[22] P. Muhlschlegel, H.-J. Eisler, O. J. F. Martin, B. Hecht, and D. W. Pohl, "Resonant optical antennas," *Science*, vol. 308, no. 5728, pp. 1607–1609, June 2005.

[23] Y. Alaverdyan, B. Sepulveda, L. Eurenius, E. Ollson, and M. Kall, "Optical antennas based on coupled nanoholes in thin metal films," *Nature Phys.*, vol. 3, pp. 884–889, December 2007.

[24] H. Kazemi, G. Nagy, L. Tran, E. Grossman, E. R. Brown, A. C. Gossard, G. D. Boreman, B. Lail, A. C. Young, and J. D. Zimmerman, ""Ultra sensitive ErAs/InAlGaAs direct detectors for millimeter wave and THz imaging applications"," in *IEEE Microwave Theory and Techniques Symposium*, vol. 8, no. 5, 2007, pp. 1367–1370.

[25] H. Kazemi, K. Shinohara, G. Nagy, W. Ha, B. Lail, E. Grossman, G. Zummo, W. R. Folks, J. Alda, and G. Boreman, ""First THZ and IR characterization of nanometer-scale antenna-coupled InGaAs/InP Schottky-diode detectors for room temperature infrared imaging"," in *Proc. SPIE*, vol. 6472, 2007, pp. 65 421J–1 – 65 421J–4.

[26] P. B. Johnson and R. W. Christy, "Optical constants of noble metals," *Phys. Rev. B*, vol. 6, no. 12, pp. 4370–4379, December 1972.

[27] D. E. Aspnes and A. A. Studna, ""Dielectric functions and optical parameters of Si, Ge, GaP, GaAs, GaSb, InP, InAs, and InSb from 1.5 to 6.0 eV"," *Phys. Rev. B*, vol. 27, no. 2, pp. 985–1009, January 1983.

[28] E. D. Palik, Ed., *Handbook of Optical Constants of Solids*. Orlando, FL: Academic Press, 1985.

[29] A. Taflove and S. Hagness, *Computational Electrodynamics: The Finite-Difference Time-Domain Method*, 2nd ed. Norwood, MA: Artech House, 2000.

[30] A. D. Rakic, A. B. Djurisic, J. M. Elazar, and M. L. Majewski, "Optical properties of metallic films for vertical-cavity optoelectronic devices," *Appl. Opt.*, vol. 37, no. 22, pp. 5271–5283, August 1998.

[31] J. Kennedy and R. C. Eberhart, *Swarm Intelligence*. Morgan Kaufmann Publishers, Academic Press, 2001.

[32] Z. Bayraktar, P. L. Werner, and D. H. Werner, "The design of minature three-element stochastic Yagi-Uda arrays using particle swarm optizmation," *IEEE Antennas and Wireless Propagation Letters*, vol. 5, no. 1, pp. 22–26, December 2006.

[33] D. W. Boeringer and D. H. Werner, "Particle swarm optimization versus genetic algorithms for phased array synthesis," *IEEE Trans. Antennas Propag.*, vol. 52, no. 3, pp. 771–779, July 2007.

[34] D. F. Kelley, T. J. Destan, and R. J. Luebbers, "Debye function expansions of complex permittivity using a hybrid particle swarm-least squares optimization approach," *IEEE Trans. Antennas Propaga.*, vol. 55, no. 7, pp. 1999–2005, July 2007.

[35] L. Rayleigh, "On the dispersion of light by a dielectric cylinder," *Phil. Mag.*, vol. XXXVI, no. 215, pp. 365–376, 1918.

[36] M. Kerker, *The Scattering of Light and Other Electromagnetic Radiation.* New York, NY: Academic Press, 1969.

[37] C. F. Bohren and D. R. Huffman, *Absorption and Scattering of Light by Small Particles.* New York, NY: Wiley, 1983.

[38] C. A. Balanis, *Advanced Engineering Electromagnetics.* New York, NY: Wiley, 1989.

[39] J. R. Wait, "Scattering of a plane wave from a circular dielectric cylinder at oblique incidence," *Canadian J. Phys.*, vol. 33, pp. 189–195, 1955.

[40] J. F. Owen and R. K. Chang, "Internal electric field distributions of a dielectric cylinder at resonance wavelengths," *Optics Letters*, vol. 6, no. 11, pp. 540–542, November 1981.

[41] R. Ruppin, "Electromagnetic energy inside an irradiated cylinder," *J. Opt. Soc. Am. A*, vol. 15, no. 7, pp. 1891–1895, July 1998.

[42] I. S. Gradshteyn and I. M. Rzyhik, Eds., *Table of Integrals, Series, and Products*, 6th ed. San Diego, CA: Academic Press, 2000, p. 624.

[43] J. E. Raynolds, B. A. Munk, J. B. Pryor, and R. J. Marhefka, "Ohmic loss in frequency-selective surfaces," *J. Appl. Phys.*, vol. 93, no. 9, pp. 5346–5358, May 2003.

[44] S. Ramon, J. R. Whinnery, and T. van Duzer, *Fields and Waves in Communication Electronics.* New York, NY: Wiley, 1965.

[45] L. C. Andrews, *Special Functions of Mathematics for Engineers*, 2nd ed. Oxford: Oxford University Press, 1998.

[46] R. W. P. King, *Electromagnetic Engineering, Vol. I Fundamentals*, 1st ed. Oxford: McGraw-Hill, 1945.

[47] R. F. Harrington, "Matrix methods for field problems," *Proc. of the IEEE*, vol. 55, no. 215, pp. 136–149, February 1967.

[48] ——, *Field Computation by Moment Methods*. Malabar, FL: Robert E. Krieger Publish Company, 1968.

[49] W. L. Stuzman and G. A. Thiele, *Antenna Theory and Design*. New York, NY: Wiley, 1981.

[50] *FEKO. EM Software and Systems-S.A.*, [Online] Available: www.emss.co.za.